ACS APPLIED MATERIALS & INTERFACES

www.acsami.org

Research Article

ECM-Mimetic CoMn-LDH Integrated PCL/PAAm Nanofibrous Hydrogel for Effective Multifunctional Drug Delivery and Fenton-Like Chemodynamic Cancer Therapy

Neeraja Bose,[○] Kumar Gokulkumar,[○] Shih-Hsuan Chen,[○] Ramalingam Mahaan,[○] Dheepthy Fabius Suresh,[○] P Varatharajan, Ganesh Munuswamy Ramanujam,[*] and Kun-Mu Lee[*]

Cite This: *ACS Appl. Mater. Interfaces* 2026, 18, 36547−36565

Read Online

ACCESS | Metrics & More | Article Recommendations | Supporting Information

Downloaded via CHANG GUNG UNIV on July 13, 2026 at 05:47:07 (UTC).
See https://pubs.acs.org/sharingguidelines for options on how to legitimately share published articles.

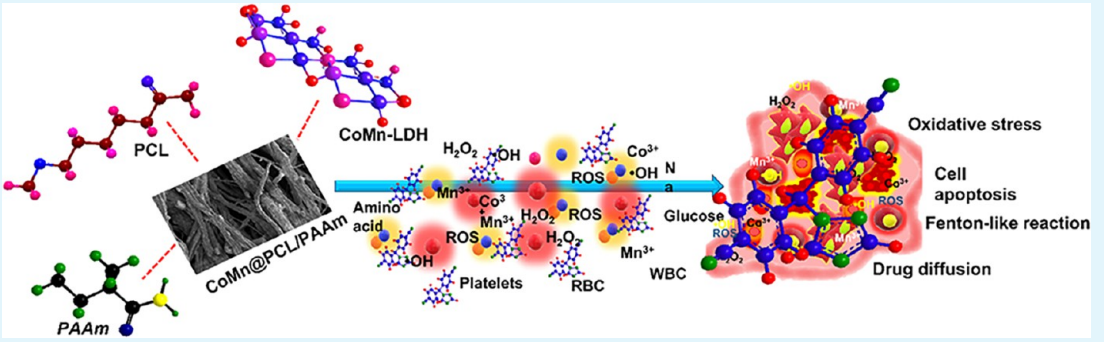

ABSTRACT: Conventional localized drug delivery systems (DDS) and chemodynamic therapy (CDT) platforms often lack structural integrity, hydration-mediated transport control, and architectures capable of sustaining redox activity at tumor sites. Here, we report a hybrid nanofibrous hydrogel that integrates CoMn layered double hydroxide (CoMn-LDH) within electrospun polycaprolactone (PCL) fibers, followed by a polyacrylamide (PAAm) hydrogel coating to construct a localized, ECM-mimetic therapeutic platform with dual functionality. Unlike Conventional CDT systems that treat drug delivery and catalytic activity independently, this design integrates a hydrated diffusion network with redox-active centers within a single architecture. The CoMn@PCL/PAAm HNF exhibits enhanced wettability of 26.4° and pronounced swelling-assisted transport, enabling sustained and non-Fickian release with cumulative release of 96.99%, 86.77%, and 97.83% at pH 6.2, 7.4, and 8.8, respectively. Furthermore, the system promotes peroxide-activated ROS generation, enhances intracellular oxidative stress, and induces apoptosis-mediated cytotoxicity against HuH7 and SiHa cells, with inhibition rates of 64.73% and 52.03%, respectively, while remaining nonhemolytic. These results indicate that interface-engineered transport reaction coupling governs both drug diffusion and ROS generation, highlighting the potential of CoMn@PCL/PAAm HNF for CDT integrated implantable anticancer applications with reduced system toxicity.

KEYWORDS: *chemodynamic therapy, COMn-LDH, electrospun, hydrogel, ECM-mimetic, catalytic activity, oxidative stress, apoptosis, and nonhemolytic*

1. INTRODUCTION

Chemodynamic and Photodynamic therapy (CDT and PDT) are widely emerging and appreciated invasive and noninvasive treatment methods for cancer.[1,2] These procedures are known to cause minimal damage to normal tissues and inactivation of multidrug resistance. These techniques accelerate the decomposition of hydrogen peroxide (H_2O_2) by metal ions, generating highly toxic reactive oxygen species (ROS) via Fenton-like reactions.[3,4] The generated ROS will break redox hemostasis and initiate oxidative damage to biomolecules such as lipids, mitochondria, DNA, and proteins, which significantly contribute to cancer cell death. The decomposition of H_2O_2 produces OH radicals that increase its concentration in cancer cells more than in normal cells (100 μM to 1 mM) and cause mitochondrial malfunction via Fenton-like reaction.[5] The produced •OH is a potent oxidant that will rupture the organelles of tumor cells, causing tumor cell apoptosis.[6]

According to the fundamental principle of CDT, which involves the utilization of transition metals, like ferrum (Fe),

Received: March 29, 2026
Revised: June 10, 2026
Accepted: June 10, 2026
Published: June 25, 2026

© 2026 American Chemical Society

https://doi.org/10.1021/acsami.6c06324
ACS Appl. Mater. Interfaces 2026, 18, 36547−36565

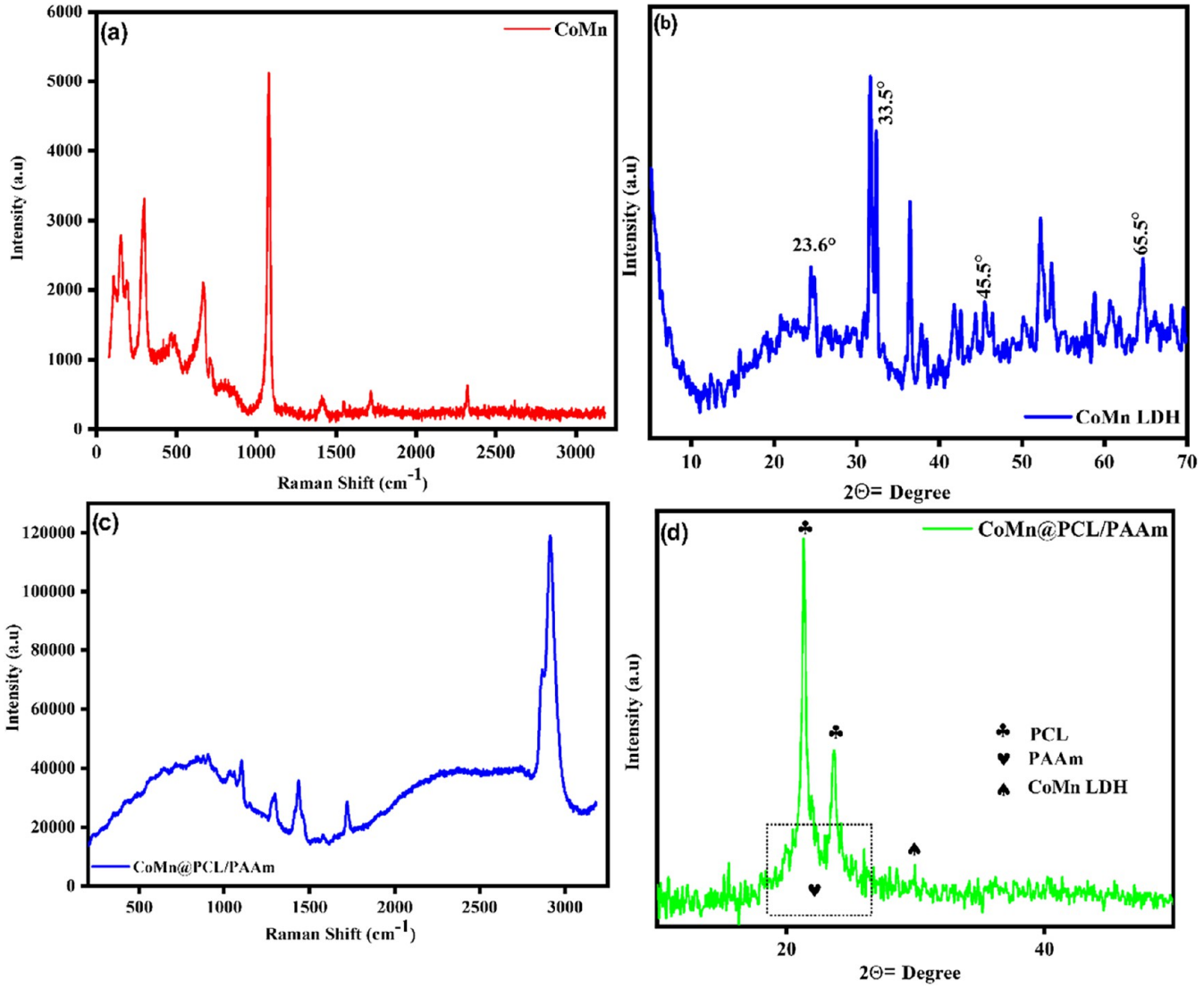

Figure 1. Raman Spectroscopic analysis: (a, c) CoMn and CoMn@PCL/PAAm HNF, and (b, d) XRD structural confirmation of CoMn-LDH and CoMn@PCL/PAAm HNF.

manganese (Mn), cobalt (Co), and copper (Cu), these metals can catalyze the conversion of excess H_2O_2 into hydroxyl radicals ($^{\bullet}OH$) in the tumor microenvironment (TME).[7] Among inorganic nanomaterials, the 2D layered double hydroxide (LDH) nanosheets are emerging as a potential nanomaterial for biomedical applications due to their excellent biocompatibility, adjustable chemical composition, and pH-responsive degradability.[8] Those 2D Transition-metal LDH nanosheets are highly designed to inhibit cancer cells that show less rupture toward normal cells.[9] These are composed of two heterovalent transition metals that are coordinated by OH groups with eccentric physicochemical properties and a high surface-to-volume ratio.[10] LDH has highly exposed surface atoms with low coordination, which are its active sites, advantageous for triggering Fenton-like reactions with intracellular H_2O_2.[11] Co^{2+} effectively catalyzes Fenton-like reactions to convert H_2O_2 into toxic $^{\bullet}OH$ radicals, , while Mn^{4+} participates in redox reactions that facilitate H_2O_2 decomposition and O_2 generation. The concurrent depletion of intracellular GSH further amplifies oxidative stress and ROS-mediated therapeutic effects.[12] The CoMn-LDH will also have advantages such as longer bond lengths, lower bond energies that increase the reaction rates, and enhance the sensitivity in the tumor environment. Also, the CoMn-LDH will self-degrade at a faster rate and will produce extreme toxicity.[13]

The equation for the Fenton reaction is as follows

$$Co^{2+} + H_2O_2 \rightarrow Co^{3+} + {}^{\bullet}OH + OH-$$

$$Mn^{2+} + H_2O_2 \rightarrow Mn^{3+} + {}^{\bullet}OH + OH-$$

Hydrogels are an advanced delivery platform, providing high water content and flexible, viscoelastic properties that govern payload release kinetics.[14] Eventually, the gel-like network will enable sustained, localized delivery and reduce systemic toxicity.[15] As an elevation, the integration of nanofibrous hydrogel via electrospinning will mimic the extracellular matrix (ECM) topography, improve the cell adhesion, mechano-transduction, and also direct the tissue regeneration.[16] The strong attachment between the functional groups is due to the chemical interaction, such as hydrogen bonding, $\pi-\pi$ stacking, coordination, and covalent bonding.[17] They are widely used in several applications due to their high surface area, tunable porosity, controlled degradation rate, and easy surface

https://doi.org/10.1021/acsami.6c06324
ACS Appl. Mater. Interfaces 2026, 18, 36547−36565

modification with high biocompatibility.[18] Simultaneously, the drugs can be infused into a nanofibrous hydrogel, which can retain the bioactivity of the drug by a controlled release profile.[19] Nanofibrous hydrogel with Polyacrylamide (PAAm) will have superior mechanical properties and structural stability. PAAm is nontoxic compared to other natural macromolecules like collagen and hyaluronic acid. It is also said to be less degradable by bioenzymes and has a longer degradation time, making it highly useful in implantation techniques.[20,21]

Conventional drug delivery systems (DDSs), including nanoformulations, thin films, and micellar systems, often fail to maintain structural integrity, catalytic accessibility to endogenous H_2O_2, and sustained therapeutic performance within the tumor site. Though the CoMn-LDH has Fenton-like activity, its practical implementation remains limited by poor retention at the target site, lack of mechanical stability, and uncontrolled leaching of active species.[22] We report an ECM-mimetic nanofibrous hydrogel platform that simultaneously optimizes diffusion-governed drug transport and redox-mediated catalytic activity within a single architecture. The integration of CoMn-LDH in PCL fibers, followed by a PAAm hydrogel coating, provides a structure that preserves exposed redox-active sites by enabling hydration regulation transport. This multifunctional combination provides sustained, non-Fickian drug release with effective peroxide activation by linking polymer relaxation, interfacial wettability, and catalytic ROS generation. This approach can demonstrate diffusion control and catalytic functionality without compromising structural stability, providing a material-level strategy for localized CDT with anticancer therapy with lowered systemic toxicity (Table S1, literature survey for previous formulations)

2. EXPERIMENTAL MATERIALS AND METHODS

A complete description of the used chemicals and instrumentation techniques is detailed in the Supporting Information.

2.1. Synthesis of CoMn-LDH

Cobalt(II) chloride hexahydrate ($CoCl_2{\cdot}6H_2O$, 10 mM) and Manganese(II) chloride (MnC_{22}, 5 mM) were dissolved in 50 mL of deionized (DI) water. Urea (NH_2CONH_2, 25 mM) was then added to the precursor solution.[23] The mixture was vigorously stirred for 30 min to obtain a homogeneous solution and subsequently transferred into a 100 mL Teflon-lined stainless-steel autoclave. The hydrothermal reaction was conducted at 180 °C for 12 h. After cooling to room temperature, a black precipitate was obtained, indicating the formation of CoMn-LDH. The product was collected and washed three times each with DI water and ethanol, and then dried at 80 °C for 24 h.

2.2. Fabricating CoMn-LDH-Loaded PCL/PAAm Nanofibrous Hydrogel

A 10 wt % poly(ε-caprolactone) (PCL) electrospinning solution was prepared by dissolving PCL in 18 mL of *N*-methyl-2-pyrrolidone (NMP) at 80 °C under vigorous stirring until a homogeneous solution was obtained. During dissolution, 1.0 g of the as-prepared CoMn-LDH and 250 mg of letrozole were added to the polymer solution, followed by stirring at room temperature for 4−6 h to obtain a uniformly dispersed solution. The resulting solution was left to deaerate overnight to remove trapped air bubbles. The electrospinning solution was loaded into a 20 mL glass syringe, and electrospinning was performed under the following conditions: collector rotation speed, 100 rpm; flow rate, 0.5 mL h^{-1}; applied voltage, 12 kV; and tip-to-collector distance, 15 cm. The PCL/letrozole (denoted as PCL) and CoMn-LDH-loaded PCL/letrozole (denoted as CoMn@PCL) nanofibrous mats were fabricated. Finally, a 5 wt % polyacrylamide (PAAm) gel was prepared using DI, added along with 2 wt % ethylenediamine, and allowed to rest for 30 min. The prepared CoMn@PCL NFs were immersed in the gel-like mixture and incubated for 6 h. The coated CoMn@PCL/PAAm HNF were oven-dried for 30 min.[23,24] All prepared nanofibrous mats were stored in sealed zip-lock bags until further characterization.

3. RESULT AND DISCUSSION

3.1. Functional Groups and Structural Characterization

3.2. Raman Spectroscopic Analysis

Raman spectroscopy confirmed the structural fingerprints of PCL and the changes induced by the incorporation of CoMn-LDH and PAAm within the hybrid matrix. As shown in Figure 1a, the CoMn-LDH spectrum exhibits several bands in the low- and midwavenumber regions that are characteristic of metal−oxygen lattice vibrations. In particular, the bands below 700 cm^{-1} are assigned to Co−O, Mn−O, and M−OH vibrational modes, indicating the presence of a hydroxylated mixed-metal inorganic framework. The intense band at 1068 cm^{-1} is consistent with the symmetric stretching vibration of interlayer or surface carbonate species, while the band near 669 cm^{-1} is attributed to carbonate bending modes. Such carbonate-related features are commonly observed in layered double hydroxide or hydroxide-rich metal systems containing carbonate and support the formation of a hydroxylated Co/Mn layered structure.[25]

In Figure S1, both pristine PCL and CoMn@PCL nanofibers exhibit the characteristic semicrystalline Raman fingerprint of PCL, confirming preservation of the polymer backbone after CoMn-LDH incorporation. The bands at 910−1098 cm^{-1} are assigned to C−COO, C−C, and C−O−C vibrations of the polyester backbone, while the 1300−1420 cm^{-1} region corresponds mainly to CH_2 twisting and bending modes, reflecting the aliphatic nature of PCL. The strong band near 1720−1730 cm^{-1} is attributed to ester carbonyl stretching, and the intense peak around 2915 cm^{-1} arises from CH_2 stretching vibrations. After the addition of CoMn-LDH, the main PCL bands remain clearly visible, indicating that the polymer structure is not disrupted. However, slight band broadening, local intensity redistribution, and reduced sharpness in the fingerprint region suggest interfacial interactions between the inorganic phase and the polymer matrix. Weak shoulders in the low-wavenumber region may be associated with Co−O/Mn−O vibrations of the CoMn phase, although the dominant polymer bands partially mask these. A minor shift or broadening of the carbonyl band further indicates local environmental changes and possible intermolecular interactions following filler incorporation.

In contrast, the CoMn@PCL/PAAm HNF spectrum shown in Figure 1c becomes markedly broader and more diffuse, indicating the formation of a more complex organic−inorganic network. The broad envelope between 800 and 1800 cm^{-1} likely originates from overlapping contributions of PCL ester vibrations and PAAm amide-related modes, while the strong band near 2915 cm^{-1} remains attributable to aliphatic C−H stretching of PCL.[26] The reduced visibility of CoMn-related bands in the HNF sample suggests that the inorganic phase is effectively embedded within the polymer/hydrogel matrix. Overall, the pronounced band broadening is consistent with enhanced intermolecular interactions, particularly hydrogen bonding between hydroxylated CoMn surfaces and PAAm

https://doi.org/10.1021/acsami.6c06324
ACS Appl. Mater. Interfaces 2026, 18, 36547−36565

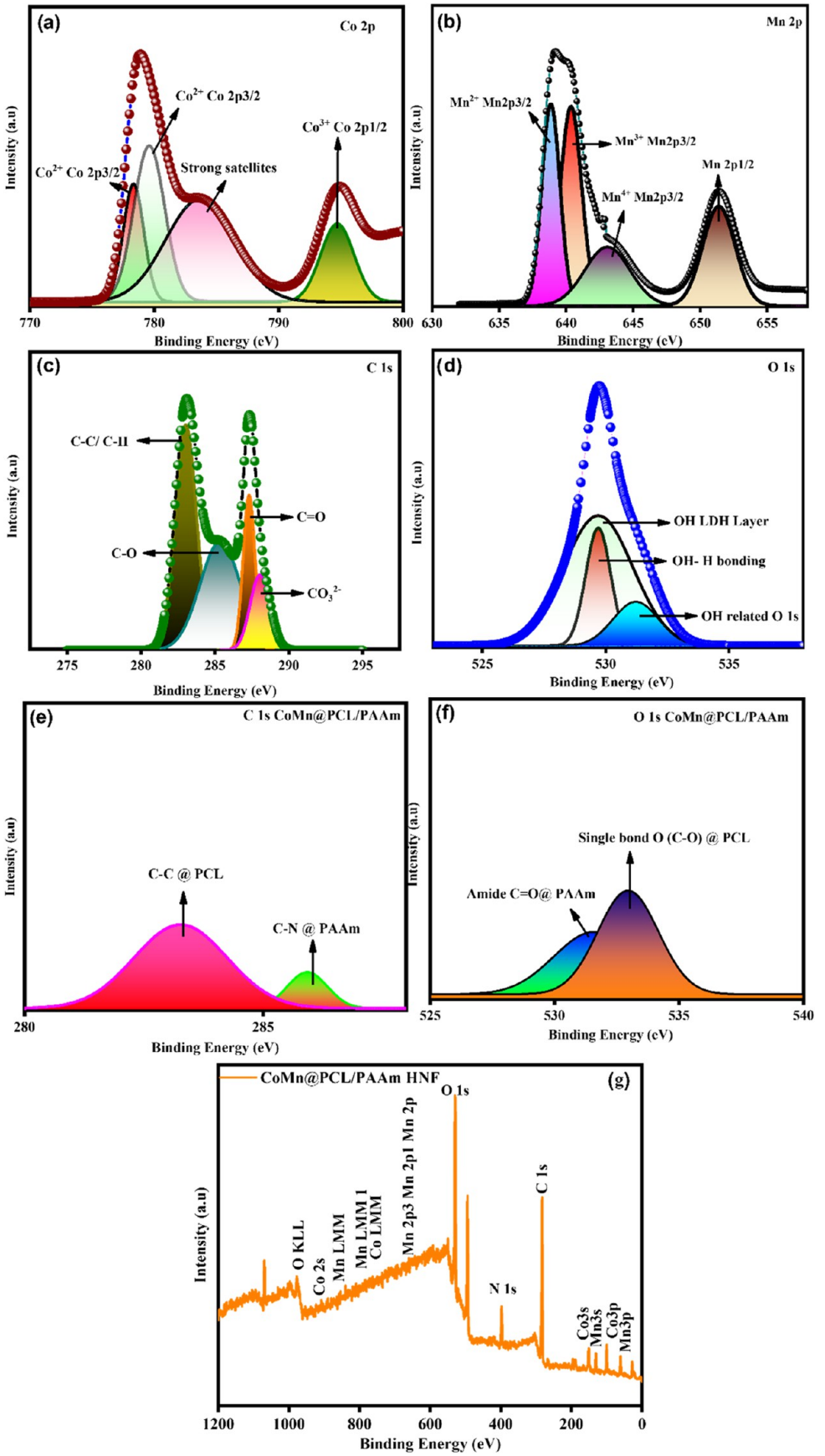

Figure 2. XPS spectra of CoMn-LDH and CoMn@PCL/PAAm: (a) Co 2p, (b) Mn 2p, (c) C 1s, (d) O 1s, (e) C 1s of CoMn@PCL/PAAm, (f) O 1s of CoMn@PCL/PAAm HNF, and (g) survey spectrum of CoMn@PCL/PAAm HNF.

https://doi.org/10.1021/acsami.6c06324
ACS Appl. Mater. Interfaces 2026, 18, 36547−36565

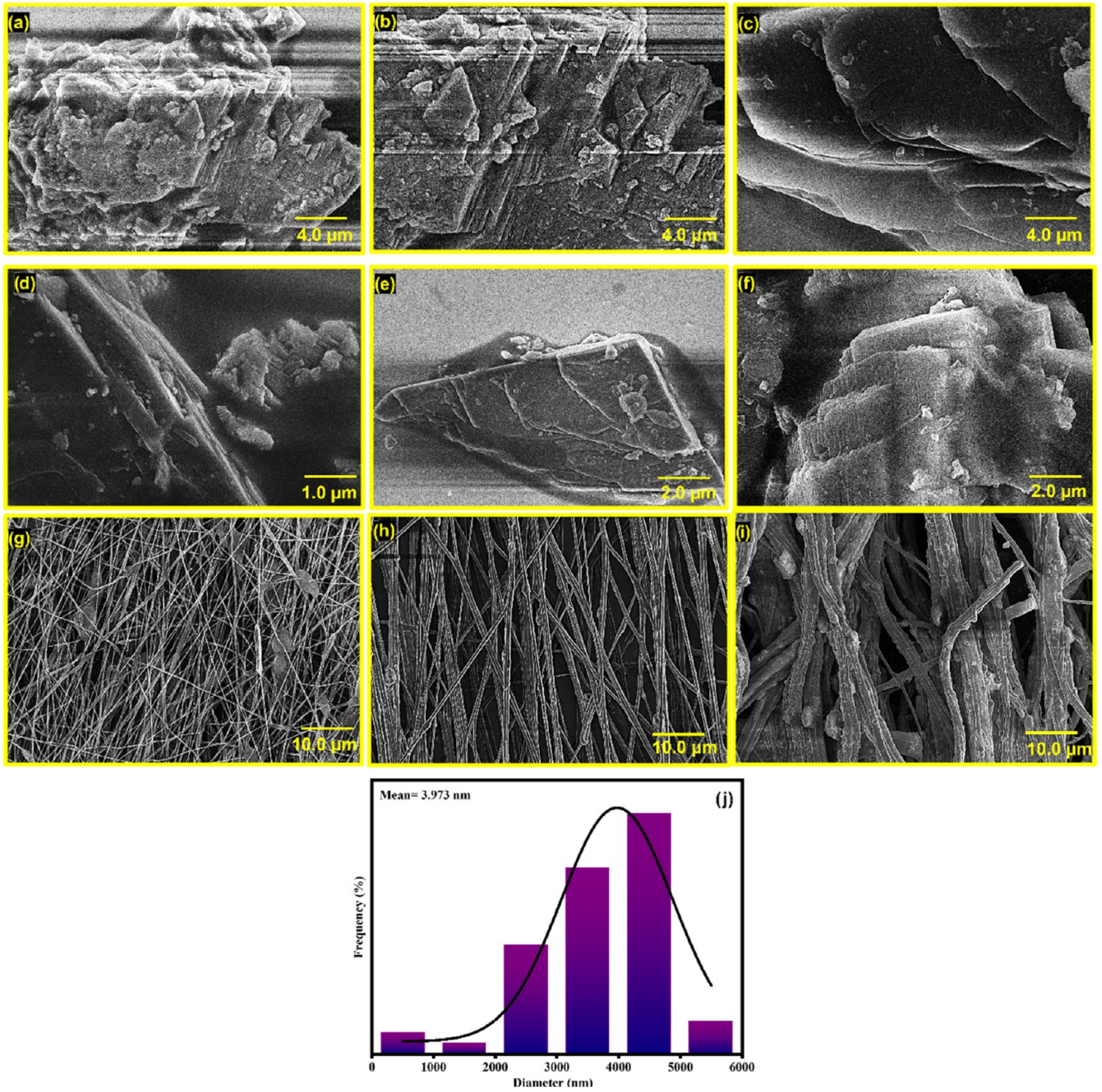

Figure 3. Morphological analysis via SEM: (a–f) CoMn-LDH layered arrangement, (g) PCL NF, (h) CoMn@PCL NF, (i) CoMn@PCL/PAAm HNF, and (j) histogram of CoMn@PCL HNF.

amide groups, as well as dipole–dipole interactions involving the carbonyl groups of PCL.[27] Therefore, the Raman results confirm successful integration of CoMn into the PCL/PAAm hybrid matrix while preserving the essential structural identity of both the inorganic and polymeric components.

3.3. XRD Structural Confirmation

The pristine PCL fiber shows all of the characteristic diffraction peaks, confirming that its crystallinity has been preserved from the electrospinning process, as shown in Figure S1. Additionally, the CoMn@PCL nanofiber displays both inorganic and polymeric phases, but the XRD pattern indicates that the matrix is primarily composed of the PCL backbone, as shown in Figure S1. From Figure 1b, it is clear that the synthesized CoMn-LDH exhibits diffraction peaks at 23.6°, 33.5°, 45.5°, and 65.5°, confirming the formation of a crystalline layered hydroxide phase. The peaks in the mid- to high-region suggest an ordered inorganic framework. The major diffraction peak at 33.5° confirms that the prepared material has a CoMn-LDH structure.[28] Furthermore, the hydrogel nanofiber's XRD pattern is dominated by the polymer matrix, with peaks at 21.5° and 23.9° representing the semicrystalline nature of PCL within the HNF matrix.[29] As shown in Figure 1d, the major peaks of PCL have shown a shift from 21.2° → 21.5° and 23.2° → 23.9° due to the incorporation of CoMn-LDH and PAAm. It is also notable that the XRD pattern masks the diffraction peak of PAAm due to its low concentration and the prominent crystallinity of

https://doi.org/10.1021/acsami.6c06324
ACS Appl. Mater. Interfaces 2026, 18, 36547–36565

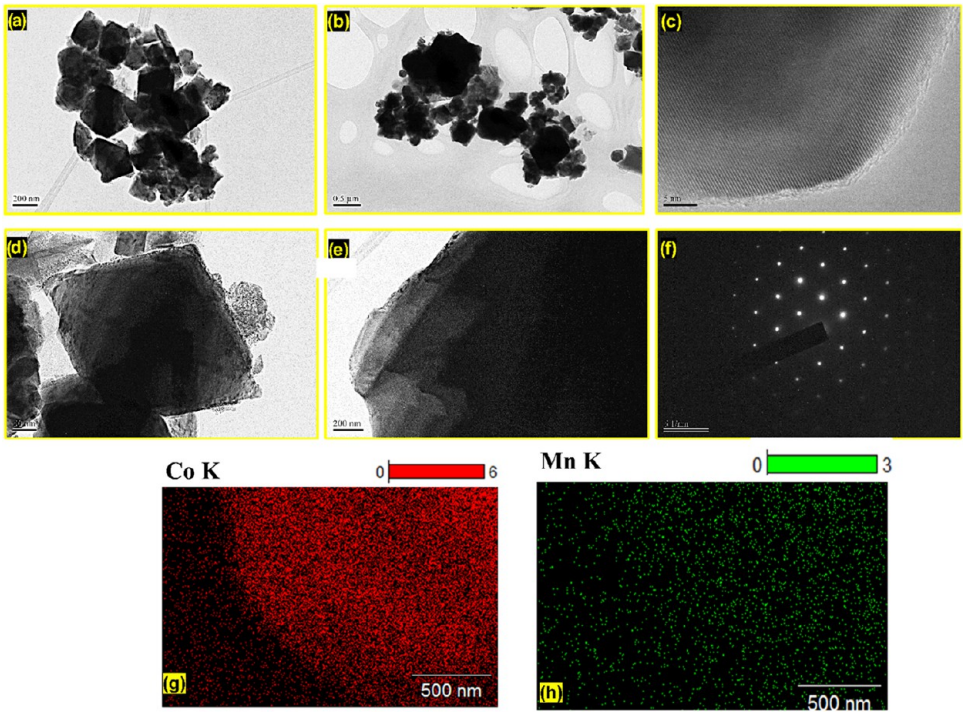

Figure 4. TEM analysis of CoMn-LDH: (a, b) TEM images of aggregated CoMn-LDH, (c) HR-TEM lattice fringe, (d, e) stacked arrangement of CoMn-LDH, (f) SAED pattern for CoMn-LDH, and (g, h) elemental mapping of CoMn-LDH.

PCL, which is also indicated by the presence of a separate amorphous halo or hump between 18° and 25°.[30] Most importantly, the HNF also shows the persistence of CoMn-LDH at 33.1°, which reflects a shift from 33.5° due to modification, indicating that the polymer HNF contains an inorganic phase. Overall, the XRD pattern indicates that any material in CoMn@PCL/PAAm HNF has not lost its nature, but is confirmed to be semicrystalline in nature.

3.4. Confirmation of Surface Elemental Composition of CoMn-LDH & CoMn@PCL/PAAm HNF

X-ray photoelectron spectroscopy (XPS) was employed to verify the surface elemental composition and oxidation states of CoMn-LDH and the CoMn@PCL/PAAm hydrogel nanofiber (HNF). As shown in Figure 2g, the survey spectrum confirms the presence of Co, Mn, C, O, and N elements. The characteristic core-level signals of Co (Co 2p and Co 3p) and Mn (Mn 2p and Mn 3p), along with intense O 1s, C 1s, and N 1s peaks, validate the successful incorporation of CoMn-LDH within the polymeric matrix. The appearance of the N 1s peak further confirms the presence of PAAm, while the dominant C 1s signal originates from the PCL/PAAm framework. The high-resolution Co 2p spectrum of CoMn-LDH (Figure 2a) exhibits two main peaks at 780 eV (Co $2p_{3/2}$) and 795 eV (Co $2p_{1/2}$), accompanied by prominent shakeup satellite features. Peak deconvolution reveals contributions from both Co^{2+} and Co^{3+} species, where the presence of intense satellite peaks is characteristic of Co^{2+} in hydroxylated environments. The coexistence of Co^{2+}/Co^{3+} indicates a mixed-valence cobalt state, which is retained after incorporation into the CoMn@PCL/PAAm HNF, suggesting preservation of redox-active sites.[31]

The Mn 2p spectrum (Figure 2b) displays Mn $2p_{3/2}$ at 641−643 eV and Mn $2p_{1/2}$ at 653−655 eV, consistent with manganese in multiple oxidation states. Deconvolution of the Mn $2p_{3/2}$ region indicates the presence of Mn^{2+}, Mn^{3+}, and Mn^{4+} species. This multivalent distribution reflects the intrinsic redox flexibility of Mn centers, which is essential for electron-transfer processes and catalytic activity in the hydrogel nanofiber system.[31] The C 1s spectrum of CoMn-LDH (Figure 2c) shows a dominant peak at 284.8 eV corresponding to C−C/C−H bonds, along with a peak at 286.0 eV attributed to C−O species. A higher binding energy component at 289−290 eV is assigned to carbonate (CO_3) species, which are commonly present in LDH interlayers. The O 1s spectrum (Figure 2d) is deconvoluted into multiple components, including lattice oxygen (M−O) at 529−530 eV, hydroxyl groups (M−OH) at 530−531 eV, and adsorbed water or surface oxygenated species at 531−533 eV. The dominance of hydroxyl-related components confirms that the LDH surface is rich in −OH functional groups, which are critical for interfacial interactions and catalytic activity.

For the CoMn@PCL/PAAm HNF matrix (Figure 2e,2f), the C 1s spectrum exhibits characteristic peaks corresponding to C−C/C−H at 284.8 eV, C−O at 286 eV, and O−C═O at 288 eV, arising from PCL ester groups and PAAm amide functionalities. The O 1s spectrum reflects contributions from ester C−O and carbonyl C═O groups of PCLs and PAAm, indicating the integrity of the polymeric network after LDH incorporation. Overall, the survey and high-resolution spectra confirm the successful integration of CoMn-LDH within the PCL/PAAm hydrogel nanofiber matrix.[32,33] Importantly, the retention of mixed-valence Co and Mn states and hydroxyl-rich surface chemistry suggests that the redox-active and interfacial properties of LDH are preserved, which is beneficial for catalytic activity, wettability, and adsorption-driven processes.

https://doi.org/10.1021/acsami.6c06324
ACS Appl. Mater. Interfaces 2026, 18, 36547−36565

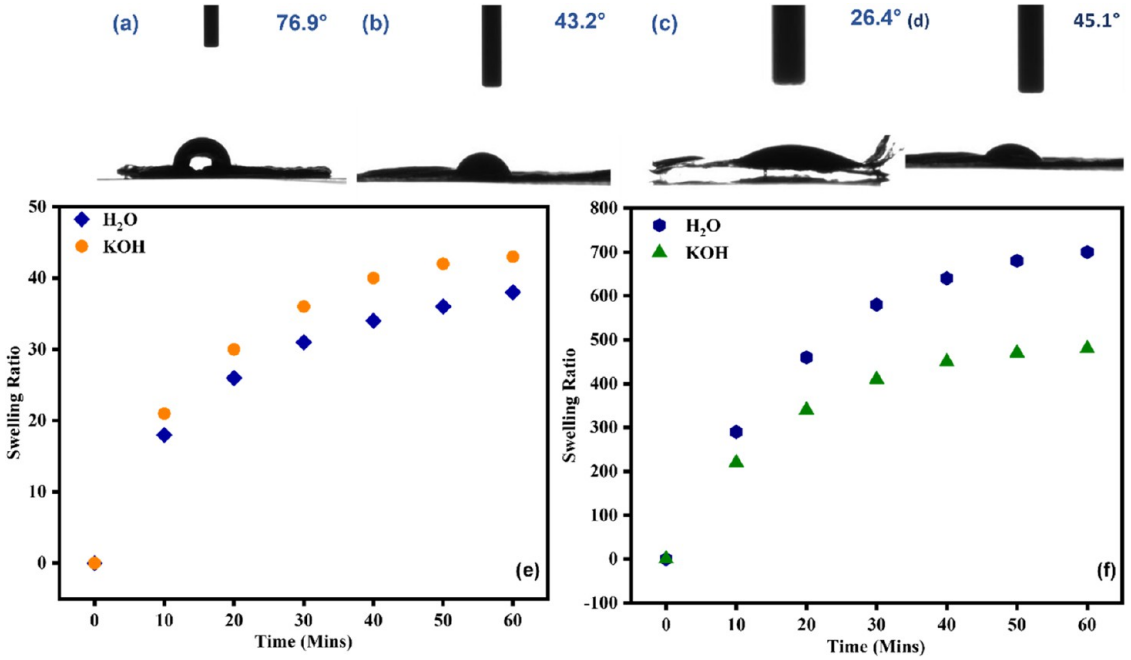

Figure 5. (a–d) Water contact angle: CoMn-LDH, PCL, CoMn@PCL, and CoMn@PCL/PAAm. (e, f) swelling ratio on CoMn-LDH and CoMn@PCL/PAAm HNF.

3.5. Morphological Confirmation of CoMn-LDH and CoMn@PCL/PAAm HNF via SEM and TEM

FESEM images confirmed the successful formation of CoMn-LDH, PCL, CoMn@PCL, and CoMn@PCL/PAAm nanofibers and hydrogel nanofibers. From Figure 3a–f results, a typical layered, plate-like morphology with fractured lamellar and sharp-edged sheets is observed, which is consistent with an LDH-type crystalline arrangement. The common appearance of platelets aggregated into clusters is also seen; this is due to the strong interlayer interactions and dry-induced stacking.[34] Such layered structures provide abundant surface-active sites, which are beneficial to catalytic redox activity. The pristine PCL nanofiber (Figure 3g) exhibits a uniform, randomly ordered, highly porous fibrous network with smooth, high surface area, and interconnected voids, which are advantageous for mass transport.[35] This porous architecture facilitates efficient diffusion pathways and enhances the drug-loading capacity. Also, the fibrous structure was retained even after incorporation of CoMn-LDH into PCL (Figure 3h), which shows a noticeable rough surface and flake-like particulates distributed, indicating a successful anchoring on the PCL surface rather than phase separation. This integration introduces redox-active sites while preserving the fibrous network that is required for effective mass transport.

After coating of PAAm (Figure 3i) in CoMn@PCL/PAAm, HNF shows thicker fibers with a textured, coated appearance and interfiber bridging, which represents the hydrogel deposition and increased surface hydration capacity.[36] The presence of a PAAm hydrogel-like layer can improve swelling behavior, which enables hydration-mediated transport. The increased fiber diameter is supported in Figure 3j, indicating a broadened fiber with an average diameter of approximately 3973 nm. The increased diameter of CoMn@PCL/PAAm HNF confirms the formation of a core–shell-like fibrous system, where the porous nanofiber network facilitates diffusion, the LDH provides redox-active sites for ROS generation, and PAAm hydrogel regulates swelling-controlled transport. This improves drug loading and pH-responsive release via electrostatic and H-bond interactions, and the PAAm hydrogel phase will swell and reduce burst release, resulting in sustained release behavior.

Figure 4a–f confirms the 2D layered morphology and crystalline nature. Figure 4a,b appears to be an aggregated plate-like crystallite forming submicron clusters that commonly resulted from LDH arrangements. Figure 4d,e shows thin lamellar plates with sharp edges and transparent regions, resulting in the formation of LDH as a nanosheet-like framework rather than dense particles. Also, Figure 4c shows lattice fringes with an interplanar spacing of 0.4 nm, evidence for the crystalline domains within the LDH plates. Further, Figure 4f represents the SAED pattern with distinct diffraction spots confirming that the CoMn-LDH obtains a single ordered crystalline structure.[37] The homogeneous distribution of Co and Mn in the prepared CoMn-LDH is confirmed by the elemental mapping as shown in Figure 4g,h.

3.6. Thermal Stability and Residual Yield

TGA analysis evaluated the thermal decomposition of prepared components (Figure S2a). The pure PCL showed its aliphatic polyester degradation with a small mass loss at lower temperature, followed by a single dominant decomposition at higher temperature corresponding to backbone degradation. The CoMn-LDH exhibits a multistep decomposition profile with an initial stage (30–200 °C) due to removal of adsorbed and interlayer water, followed by dihydroxylation and interlayer anion loss in the 200–550 °C range. This gradual mass loss resulted in the stable formation of metal oxide and a higher residual fraction. In CoMn@PCL NF (Figure S2b), three-stage decomposition was observed at 25.9–109.2 °C (loss of volatile and adsorbed species), 149.8–452.3 °C (major PCL degradation overlapped with LDH dihydroxylation/anion loss), and final decomposition stages associated with composition breakdown and residual mass loss of 6.8% with oxide formation.

https://doi.org/10.1021/acsami.6c06324
ACS Appl. Mater. Interfaces 2026, 18, 36547–36565

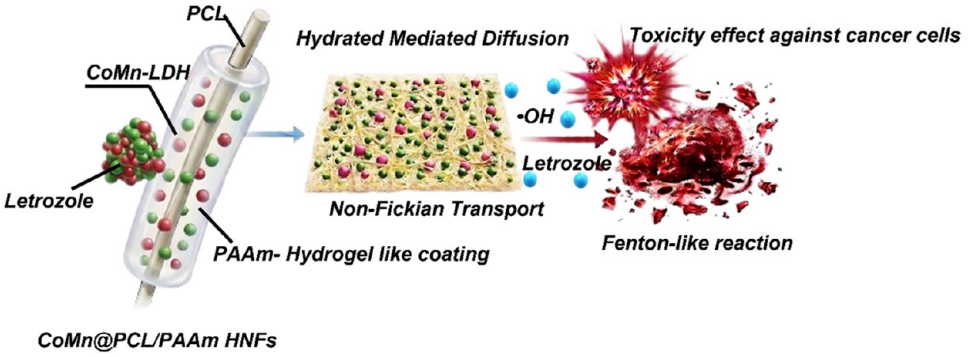

Figure 6. Schematic representation of the transport mechanism in CoMn@PCL/PAAm hydrogel nanofibers.

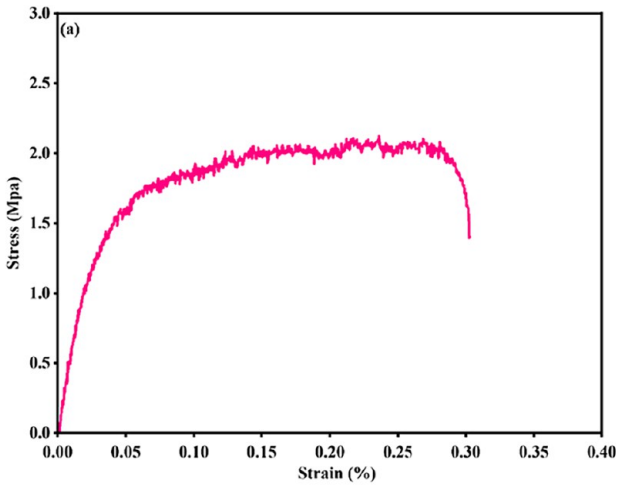

Average tensile strength [MPa]	Maximum tensile strength [MPa]	Elongation at break [%]	Young's modulus [GPa]
0.21 ± 0.01	0.23	0.30 ± 0.06	51.22 ± 2.62

Figure 7. Mechanical stress and strain curve for CoMn@PCL/PAAm HNF and its parameter.

For CoMn@PCL/PAAm HNF, there are three stages, which are observed to have initial loss of water from PAAm and LDH, at 231.2−347.0 °C, attributed to early PAAm degradation, and main degradation 347−471.8 °C due to the combination of PCL and PAAm decomposition with LDH dihydroxylation/anion loss. The final char residue is 0.25%, indicating a lower inorganic fraction compared to CoMn@PCL NF. This suggests that CoMn@PCL NF has higher residual metal oxide content that produces more redox-active sites, which are favorable for Fenton-like H_2O_2 decomposition and ROS generation, whereas the CoMn@PCL/PAAm HNF improves the diffusion and H_2O_2 transport, supporting PDT or combined CDT-PDT activity.

3.7. Water−Material Interactions: Contact Angle and Swelling

CoMn-LDH was observed to be hydrophilic, as shown in Figure 5a. The hydrophilic nature of CoMn-LDH is owed to the presence of −OH groups present in the metal hydroxide layers (Co−OH and Mn−OH), which act as hydrogen bond donors and acceptors, enabling the strong interaction between water molecules. The interlayer anions Co_3^{2-} and associated hydrated water enhance its affinity toward the aqueous environment.[38] These −OH-rich layered structures provide high surface polarity, facilitating water adsorption and supports hydration driven process. Further, the static water contact angle measurement of PCL and its composite film was measured as shown in Figure 5b−d. The PCL film shows a hydrophobic nature of 76.9°, due to the aliphatic polyester backbone, dominated by nonpolar $-(CH_2)_{5-}$ segments.[39] After the incorporation of CoMn on PCL, it was reported to be slightly hydrophilic due to the hydroxyl-rich CoMn-LDH and nanofibrous arrangement, which was measured to be 43.2°, indicating improved surface wettability due to the introduction of the −OH group and surface roughness. The CoMn@PCL/PAAm film was observed to be highly hydrophilic with a measurement of 26.4°, which can be due to the improved surface polarity due to the hydroxyl-rich CoMn-LDH and polar amide groups of PAAm.[40]

While comparing the swelling ratio of the prepared materials for 60 min is shown in Figures 5e,f and S3. Thus, CoMn@PCL/PAAm was observed to have a swelling ratio greater than that of other systems. The increase in the swelling ratio arose from the hydrophilic and three-dimensional PAAm hydrogel network combined with the OH-rich surface of CoMn-LDH. The amide group of $(-CONH_2)$ in PAAm provides a strong hydrogen bond with water, enabling rapid absorption and retention within the polymer network. Simultaneously, the CoMn-LDH introduces abundant −OH groups and interlayer ionic species, which further promote water adsorption and

https://doi.org/10.1021/acsami.6c06324
ACS Appl. Mater. Interfaces 2026, 18, 36547−36565

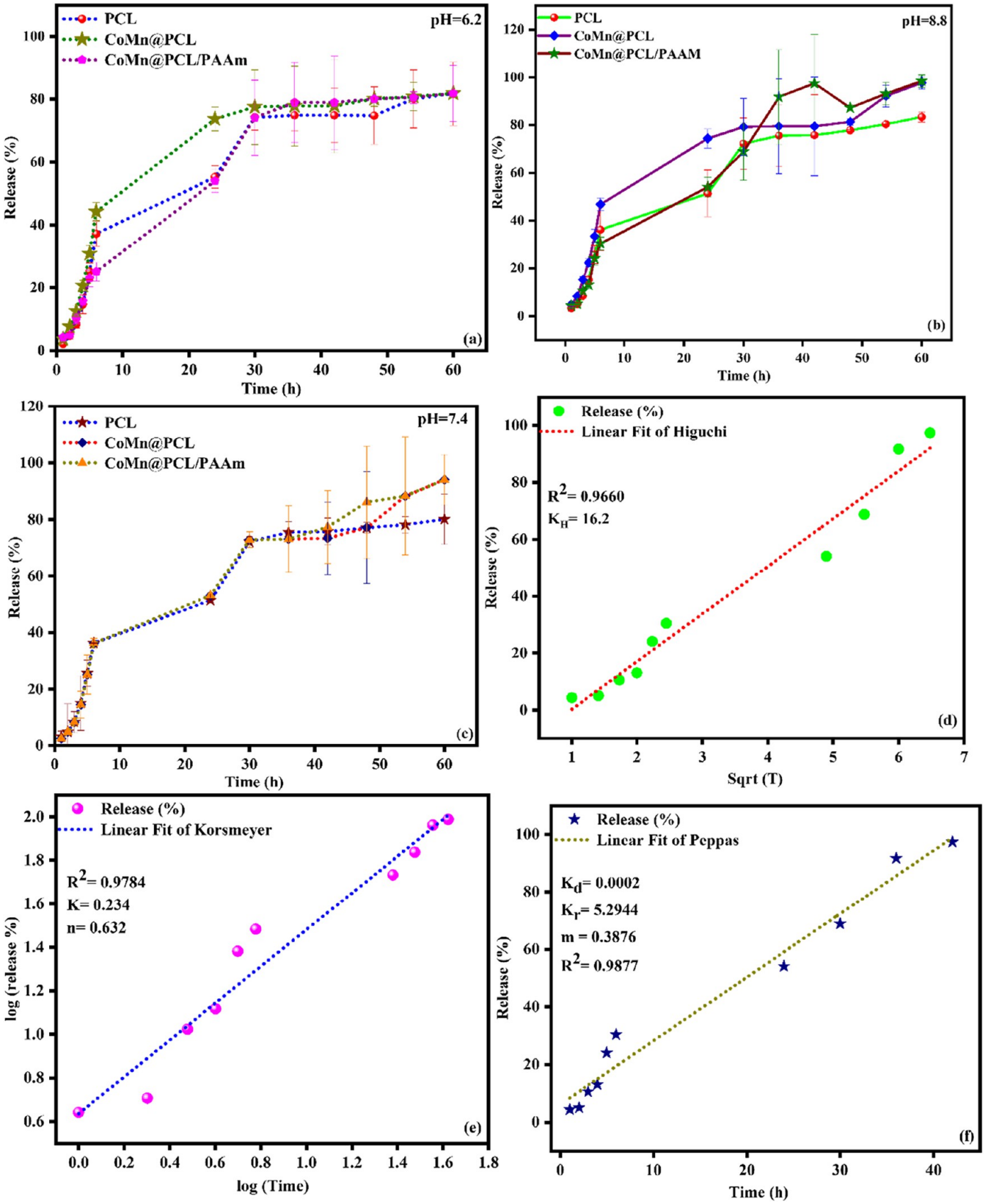

Figure 8. (a–c) In vitro drug release activity of PCL, CoMn@PCL, and CoMn@PCL/PAAm HNF at pH 6.2, 8.8, and 7.4, and (d–f) Higuchi, Korsmeyer-Peppas, and Peppas-Sahlin kinetic models of CoMn@PCL/PAAm HNF.

hydration. The reduced contact angle of the composite increases the initial water infiltration at the interface. This combined effect of hydrogel swelling, LDH-induced hydrophilicity, and enhanced wettability results in an increased hydrated matrix. This enhanced hydration controls the diffusion pathways of the system, resulting in controlled drug

https://doi.org/10.1021/acsami.6c06324
ACS Appl. Mater. Interfaces 2026, 18, 36547–36565

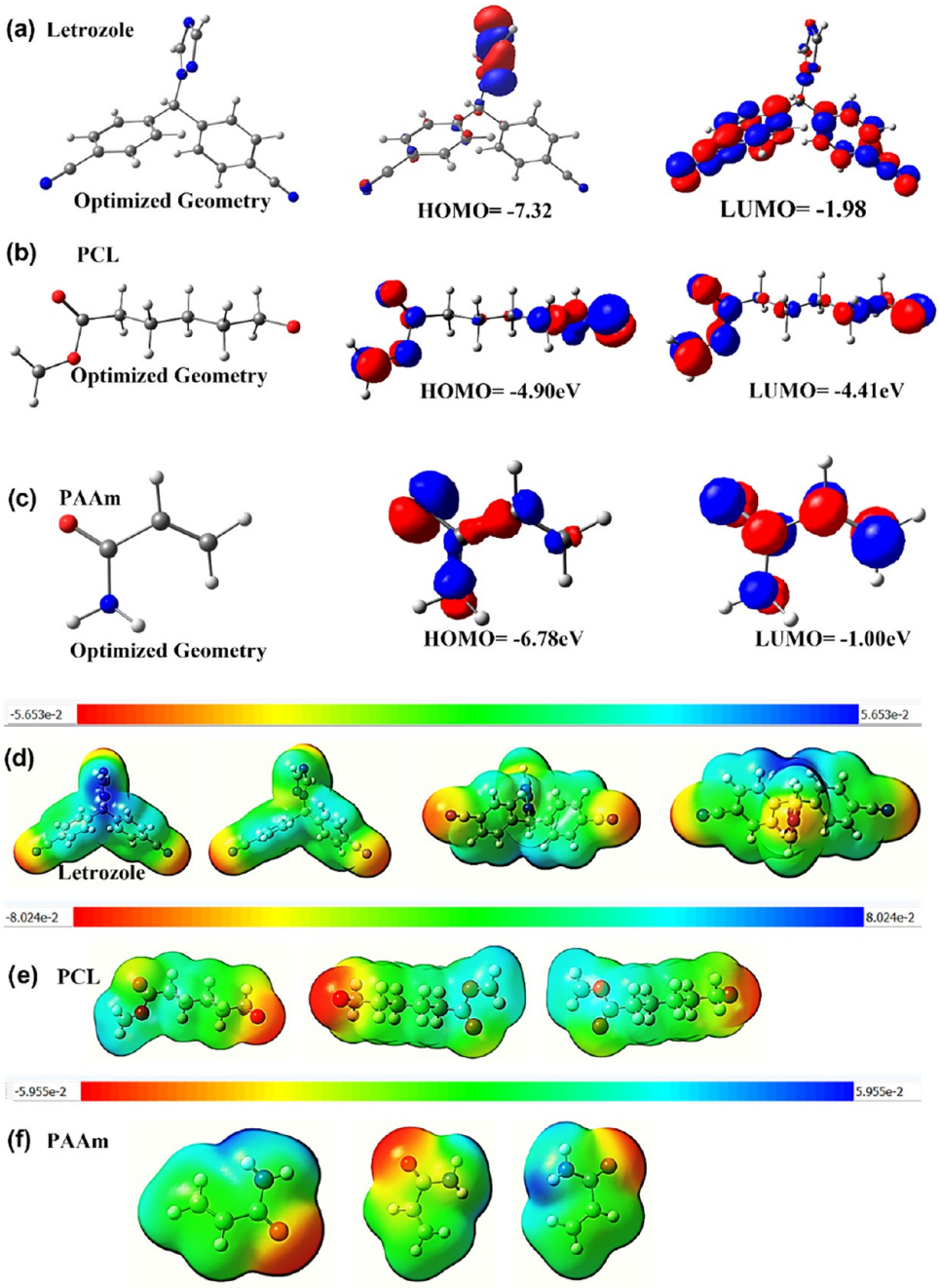

Figure 9. (a–c) Optimized geometries of Letrozole, PCL, and PAAm and Frontier Molecular orbitals, and (d–f) electrostatic potential map illustrating charge distribution representing electron-rich sites and electron-deficient sites of Letrozole, PCL, and PAAm.

release and may result in sustained release, which shows a structure–property–function relationship (Figure 6).

3.8. Mechanical Stress and Strain Curve of CoMn@PCL/PAAm HNF

The stress–strain behavior of CoMn@PCL/PAAm HNF is presented in Figure 7, showing an elastomeric polymeric network response with an initial elastic region followed by gradual plastic deformation before fracture. The continuous increase in stress with strain indicates an effective load transfer along the interconnected fibrous structure without immediate brittle failure. The scaffold showed an average tensile strength of 0.21 MPa and a maximum tensile strength of 0.23 MPa, illustrating adequate mechanical stability under applied loading. Also, the improved tensile behavior is attributed to the incorporation of CoMn-LDH within the PCL/PAAm matrix, where the nanosheets act as reinforcing domains that stop polymer chain mobility and promote uniform stress distribution. PAAm contributes intermolecular cohesion via hydrogen bond interactions, while the PCL shows flexibility and fibrous continuity.

The elongation at break value of 0.30 results in good ductility and deformability before rupture, suggesting strain accommodation via gradual fiber rearrangement and polymer chain extension rather than sudden fracture. In addition, the Young's modulus of 51.22 MPa confirms the relatively stiff nature of the scaffold and reflects improved resistance to elastic deformation due to enhanced interfacial interaction between

https://doi.org/10.1021/acsami.6c06324
ACS Appl. Mater. Interfaces 2026, 18, 36547–36565

CoMn-LDH and the polymer matrix. Overall, the CoMn@PCL/PAAm HNF result with a balanced combination of stiffness, tensile strength, and flexibility is suitable for biomedical and anticancer therapy.

3.9. In Vitro Drug Release Behavior

The in vitro release profiles of PCL, CoMn@PCL, and CoMn@PCL/PAAm NFs and HNF were determined at pH 6.2, 7.4, and 8.8 for up to 42 h, respectively. All of the matrices have shown a biphasic profile with rapid initial release and ended with a slow plateau at extended times. This can be due to the drug that is located near the fiber surface or pores and follows a diffusion from the deep region of the matrix. This shows that drug release is governed by diffusion-controlled transport within the fibrous network. From Figure 8a, it is evident that the PCL exhibited an average early release of 36−37% at each pH value at 6 h and gradually showed a higher release of 51−55% at each pH value at 24 h. At 42 h, the PCL matrix has released almost 73−75% of its loaded letrozole. The relative variation of release among all pH values shows that the release is dependent on the medium penetration and diffusion through the polyester-dominant NF rather than the pH trigger. Later, Figure 8b reveals that the profile has increased in early and overall release after the incorporation of CoMn-LDH into PCL. CoMn@PCL has shown an average of 42−46% of release after 6 h at each corresponding pH. Over an extended period, the release was noted to be 77−79% with a corresponding pH at 42 h. This can be attributed to the blending of letrozole in the polymer solution, which is not intercalated in LDH, thereby improving the transport effect by enhancing wettability and reducing diffusional resistance.[41]

In contrast, CoMn@PCL/PAAm HNF has shown extended long release, as shown in Figure 8c. Initially, the system produced a burst release from 25 to 20% in each pH until 6 h, which is comparatively lower than the CoMn@PCL NF. Over an extended time period, the system exhibited greater drug depletion at 42 h, with cumulative releases of 96.99%, 86.77%, and 97.35% at pH values of 6.2, 7.4, and 8.8. By extending the release activity to 60 h, all of the systems have shown maximum release of letrozole at pH 8.8 of 83.34%, 97.60%, and 98.34%. This is due to the presence of a highly hydrated PAAm network, which provides continuous diffusion channels and initiates sustained release. The swelling of PAAm provides a controlled diffusion barrier, thereby suppressing the burst release and enabling sustained release kinetics. The lower final release at pH 7.4 may be due to variations in solute transport under different pH and ionic strength conditions. Thus, overall release at 42 h was CoMn@PCL/PAAm > CoMn@PCL > PCL, indicating that HNF has a modest increase after incorporation of CoMn, and PAAm has shown a hydration-controlled release system. Also, it is to be said that the system is non-TME-responsive, driven by hydrogel permeability rather than specific chemical degradation of the carrier. Collectively, these results show that the fibrous system governs the diffusive route, enhanced wettability, swelling transportation, providing sustained and controlled drug delivery. This combined system highlights the potential for future chemodynamic therapeutic effects.[42]

To determine the release mechanism of CoMn@PCL/PAAm HNF, the cumulative release was fitted using Higuchi (diffusion, R^2 = 0.9660), Korsmeyer-Peppas (semiempirical, R^2 = 0.9784), and Peppas-Sahlin (mechanistic, R^2 = 0.9877) models, as shown in Figure 8d−f. Overall, the three models exhibit good linearity, indicating that transportation depends on the swelling of the polymer networks.[43] The Higuchi fit (K_H = 16.2) suggests a strong diffusion-controlled component through the hydrated matrix. Meanwhile, the Korsmeyer-Peppas exponent (n = 0.632) indicates an anomalous (non-Fickian) state, meaning diffusion occurs alongside time-dependent polymer swelling or relaxation. Conversely, the Peppas-Sahlin model provides the best fit, with a dominant relaxation constant ($K_r \gg K_d$), resulting from hydrated PAAm hydrogel and chain relaxation processes that open or maintain aqueous pathways, thereby reducing tortuosity and enabling sustained transport. Therefore, the overall release of letrozole from CoMn@PCL/PAAm HNF occurs via swelling-regulated diffusion through porous channels created by PAAm, with the PCL nanofiber maintaining structural integrity, and CoMn-LDH influencing microwettability.[44] Consequently, the CoMn@PCL/PAAm HNF exhibits an anomalous (non-Fickian) transport mechanism. Schematic representation of transport by CoMn@PCL/PAAm is shown in Figure 6.

3.10. Possible Interaction and Theoretical Validation for Possible Drug Release

The density functional theory (DFT) results in Figure 9 show an interaction model for the CoMn@PCL/PAAm NF drug delivery system. All ground-state geometries of PCL, PAAm, and Letrozole were optimized using the B3LYP functional and def2-SVP basis set in the Gaussian 16 software package.[1] The optimized geometries were confirmed to be local minima by the absence of imaginary frequencies. From Figure 9a−c, the ground-state optimized geometry of PCL, PAAm, and Letrozole shows PCL as an aliphatic chain with segmental ester functionalities and low polarity. In contrast, PAAm is more compact and highly polar, with active amide groups that can promote strong intermolecular interactions. In contrast, Letrozole exhibits a nonplanar geometry with nitrogen-rich aromatic moieties, featuring multiple sites for intermolecular interactions rather than simple planar stacking. These structural differences indicate that PAAm shows polar interactions, PCL provides diffusive support, and together they influence drug matrix interactions. Furthermore, the frontier orbital analysis of the system shown in Figure 9a−c indicates that PCL has its highest occupied molecular orbital (HOMO) (−4.90 eV) and the lowest unoccupied molecular orbital (LUMO) (−4.41 eV) localized on ester-containing segments, showing that the carbonyl regions are the most reactive sites of the polymer chain. Whereas in Letrozole, the HOMO is concentrated over the nitrogen-containing domain, while the LUMO is more delocalized over the conjugated framework. PAAm shows a deep HOMO (−6.78 eV) and a high-lying LUMO (−1.00 eV), which confirms that the coating on the CoMn@PCL NF system will be a chemically stable polar coating layer that provides more interfacial binding and hydration control than charge transfer.[45]

From the electrostatic potential (ESP) map (Figure 9d−f), the red corresponds to the nucleophilic regions and blue to the electrophilic regions. The nucleophilic regions of PCL, PAAm, and Letrozole are the ester oxygen, nitrile, triazole nitrogen region, and amide oxygen-rich region, whereas the electrophiles are noted to be the polarized carbonyl carbon, the hydrogen-deficient ring of Letrozole, and the amide hydrogen of PAAm. The significant intermolecular interactions will be H-bonding between PAAm's N−H and the N atoms of Letrozole, dipole−dipole interactions between the ester groups

https://doi.org/10.1021/acsami.6c06324
ACS Appl. Mater. Interfaces 2026, 18, 36547−36565

of PCLs and the polar nitrile/triazole moieties of Letrozole. In addition, the quantum chemical global reactivity parameter, as shown in Table 1, descriptor of Letrozole shows that the

Table 1. Quantum Global Reactivity Parameter

HOMO	−7.32
LUMO	−1.98
H-L Gap	5.34
global hardness η	2.67
chemical potential μ	−4.65
global softness σ	0.37
absolute electronegativity χ	4.65

HOMO and LUMO energy values yield a high energy gap of 5.34 eV. Also, it shows that the letrozole is electronically stable, less reactive, governed by noncovalent interactions than strong chemical reactivity. Also, the chemical potential shows that the system will be thermodynamically stable, and the drug is a moderately electron acceptor, which facilitates interactions with the electron-rich group of CoMn@PCL/PAAm HNF. Thus, the DFT calculations suggest that letrozole remains structurally stable during encapsulation and sustained release of the drug with ROS-initiated cancer inhibition.

3.11. Acellular Fenton Activity for ROS Generation of CoMn@PCL/PAAm HNF

The Fenton-like catalytic activity of the CoMn@PCL/PAAm hydrogel nanofiber (HNF) was evaluated using a methylene blue (MB) degradation assay (Figure 10a,b). Control groups included MB+PBS, MB + PBS + H_2O_2, and MB + PBS + H_2O_2 + IPA, where isopropanol (IPA) was used as a hydroxyl radical ($^{\bullet}OH$) scavenger. The catalytic activity was monitored by the time-dependent decrease in the MB absorbance band, which serves as an indicator of oxidative degradation under peroxide-activation conditions. In Figure 10a, MB in PBS shows a strong absorption band, while MB + PBS + HNF exhibits no comparable loss, indicating that the scaffold alone does not induce significant dye degradation in the absence of peroxide. Upon the addition of H_2O_2, the CoMn@PCL/PAAm HNF produces a progressive reduction in MB intensity from 10 to 60 min, confirming time-dependent catalytic oxidation. The persistence of measurable degradation even in the presence of IPA suggests that radical-mediated pathways are operative, with $^{\bullet}OH$ contributing substantially to the oxidation process.

In Figure 10b, the ROS-scavenging control shows that MB + PBS and MB + PBS + H_2O_2 + IPA remain largely unchanged, confirming that H_2O_2 alone does not appreciably degrade MB under these conditions. In contrast, MB + PBS + H_2O_2 + CoMn@PCL/PAAm (film) exhibits a clear time-dependent suppression of the MB absorption band at 10, 30, and 60 min, with the strongest attenuation at 60 min, evidencing sustained peroxide activation by the CoMn-containing hydrogel nanofiber. Collectively, the data support that Co/Mn redox centers in the HNF catalytically activate H_2O_2 to generate highly reactive oxygen species that oxidatively disrupt the MB chromophore, resulting in decreased absorbance. This MB degradation assay provides acellular chemical evidence that the CoMn@PCL/PAAm HNF functions as a ROS-generating substrate in peroxide-containing media, supporting its potential for chemodynamic therapy (CDT); however, it does not by itself prove anticancer efficacy and primarily validates the material's peroxide-activation capability for subsequent CDT-oriented biological studies.[2] The degradation kinetics of methylene blue were analyzed using a pseudo-first-order model (Figure S4). The linear fit relationship confirms that the reaction follows pseudo-first-order kinetics. The rate constant (k) was 0.00956 min^{-1}, indicating that the degradation is a controlled catalytic process. This suggests that PAAm hydrogel matrix modulates the diffusion of H_2O_2 and MB molecules toward the CoMn active sites, thereby regulating ROS generation. The observed behavior supports the presence of transport reaction coupling, where hydration-mediated diffusion governs catalytic activity within the nanofibrous hydrogel system.

3.12. Antibacterial Assessment via Resazurine Assay

The antibacterial activity of the NFs and HNF was evaluated via resazurine assay against *Staphylococcus aureus (Gram-positive)* and *Escherichia coli (Gram-negative)*, as shown in Figure 10c. The resazurin assay results in the bacterial metabolic viability through the reduction of nonfluorescent blue resazurine into pink fluorescent resorufin by metabolically active bacterial cells. Therefore, a reduced level of formation corresponds to lower bacterial viability and enhanced antibacterial activity.

The PCL exhibited only minimal antibacterial activity, resulting in 8.25% ± 2.52 inhibition against *S. aureus* and 7.50% ± 0.50 against *E. coli*, indicating that PCL alone is highly biologically inert toward bacterial growth. After incorporation of CoMn, the inhibition rate has slightly increased to 25.51% ± 0.62 and 12.54% ± 0.50, respectively. This originated from the redox-active Co^{2+}/Mn^{2+} catalytic centers, which can induce oxidative stress through ROS generation by damaging bacterial membranes, proteins, and intracellular biomolecules.

In contrast, CoMn@PCL/PAAm illustrated a potentially improved antibacterial activity, with an inhibition rate of 67.86% ± 0.38 against *S. aureus* and 41.94% ± 0.06 against *E. coli*. The improved bacterial inhibition is contributed to by the CoMn, PAAm, and Letrozole. The hydrophilic PAAm layer will improve the water uptake and interfacial contact between the scaffold and bacterial cells, facilitating diffusion-mediated interaction and exposing a large number of catalytically active sites.[46] Simultaneously, ROS generated from CoMn-mediated redox reaction may induce membrane lipid peroxidation, oxidative protein damage, and intracellular leakage, collectively lowering the bacterial metabolic activity as reflected in the resazurin assay. Thus, higher inhibition was observed against *S. aureus*, which has a relatively permeable, peptidoglycan-rich cell wall structure. In contrast, *E. coli* possesses an additional lipopolysaccharide having an outer membrane acting as a permeability barrier, limiting penetration of ROS and external antibacterial agents.

3.13. In Vitro Cytotoxicity Assessment by the MTT Assay

The cytotoxicity of NFs and HNF was evaluated using the MTT assay against HuH7 and SiHa cancer cell lines (Figure 10d,e). The MTT assay shows the cellular metabolic activity through the reduction of yellow tetrazolium salt (MTT) into insoluble purple formazan crystals by mitochondrial dehydrogenase enzymes in viable cells. The decrease in formazan formation shows the reduced mitochondrial activity and lower cell viability. The control sample shows negligible cytotoxicity, indicating a baseline biocompatibility under the assay conditions. Among the fabricated samples, the cell death rate at 48 h on PCL was 20.75% (HuH7), as shown in Figure 10d, and 14.86% (SiHa), as shown in Figure 10e, indicating that pristine PCL does not exhibit significant cell inhibition. After

https://doi.org/10.1021/acsami.6c06324
ACS Appl. Mater. Interfaces 2026, 18, 36547−36565

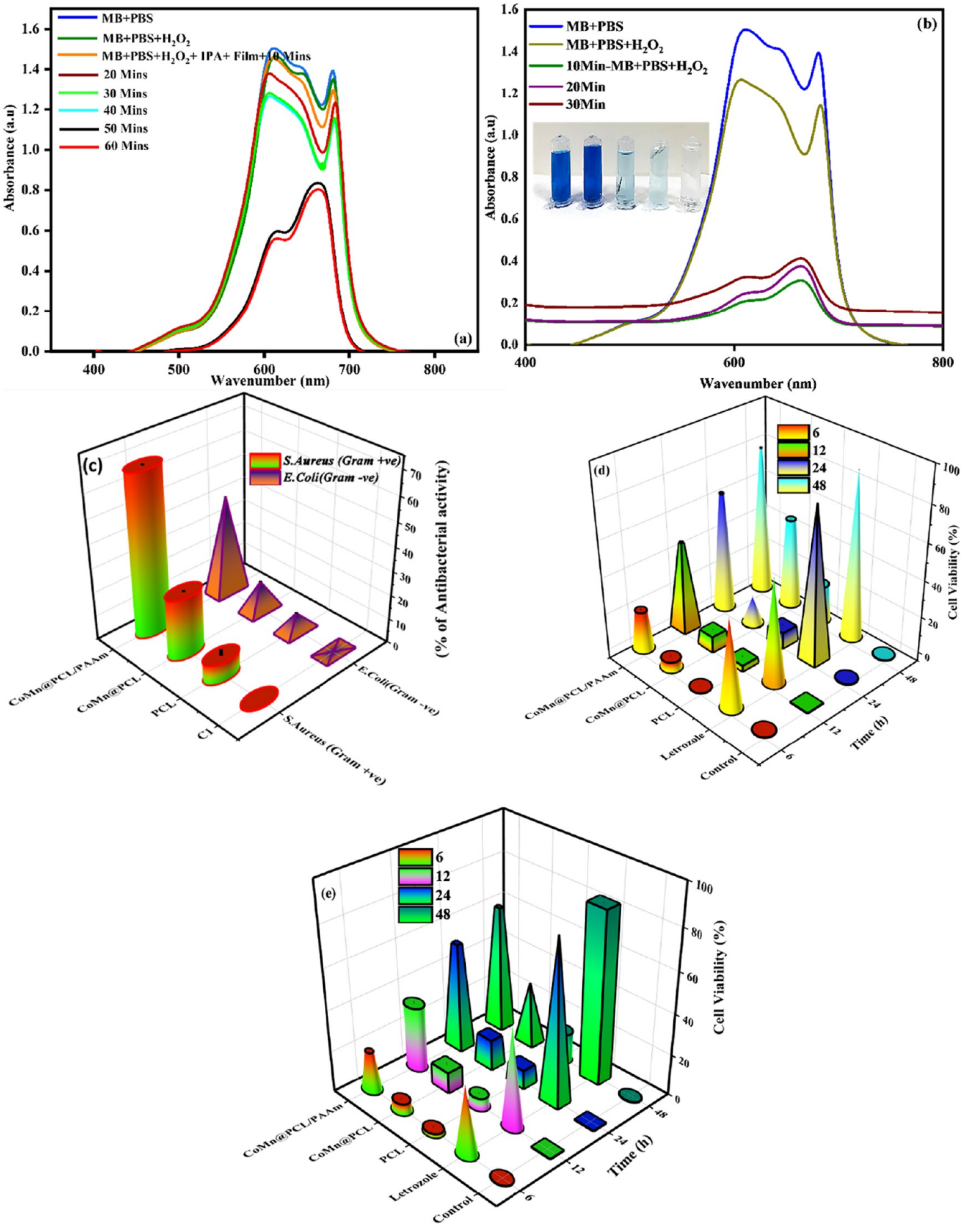

Figure 10. Fenton-like time-dependent catalytic degradation of Methylene blue by CoMn@PCL/PAAm HNF: (a) With IPA and H_2O_2, and (b) only H_2O_2. (c) Antibacterial analysis on PCL, CoMn@PCL/PAAm, and MTT cancer inhibition rate of PCL, CoMn@PCL, and CoMn@PCL/PAAm (d) against HuH7 with Mean SD = ± 0.393, n = 3, and statistically significant ($p < 0.01$ and $p < 0.001$) and (e) against SiHa with Mean SD = ± 0.0978, n = 3, and statistically significant ($p < 0.01$ and $p < 0.001$).

https://doi.org/10.1021/acsami.6c06324
ACS Appl. Mater. Interfaces 2026, 18, 36547−36565

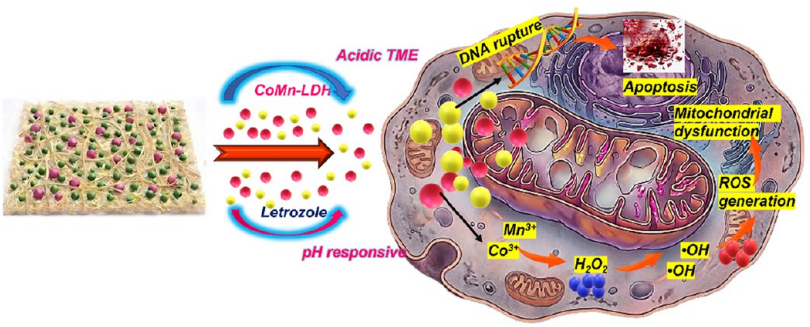

Figure 11. Schematic illustration of Fenton-like activity of CoMn@PCL/PAAm HNF on cancer cells, conversion of H_2O_2 to •OH induces oxidative damage and apoptosis.

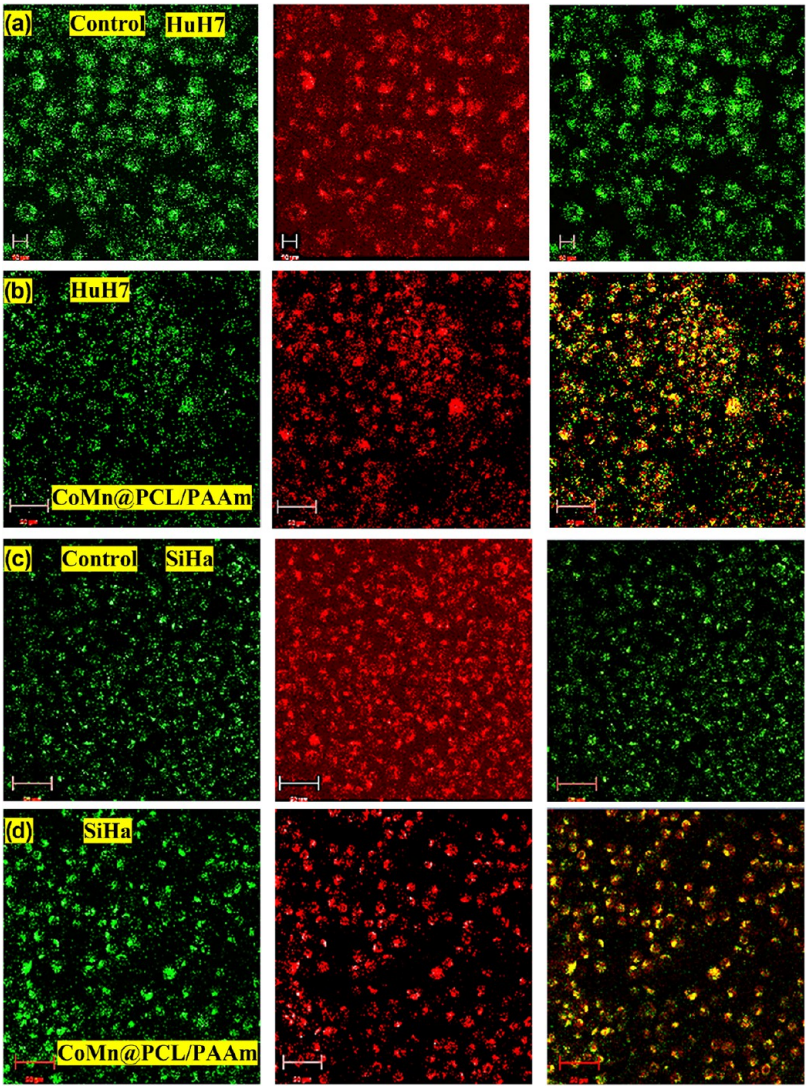

Figure 12. Apoptosis analysis on CoMn@PCL/PAAm: (a, c) control and (b, d) Ao/EtBr staining on the CoMn@PCL/PAAm film.

the incorporation of CoMn-LDH into PCL, the cell inhibition slightly increased to 48.89% (HuH7) and 30.00% (SiHa), which suggests a moderate contribution from the metal hydroxide phase, possibly due to limited ROS generation or surface-mediated interactions. This behavior can be associated with partial redox activity of Co^{2+}/Mn^{2+} centers, which may initiate mild oxidative stress without sufficient accumulation to induce significant cytotoxicity.[47]

However, in the CoMn@PCL/PAAm NFs system, a significant enhancement in cytotoxicity was observed toward HuH7 and SiHa cells, with 82.12% and 65.56% cell death, respectively. This can be attributed to the combined effects of CoMn-LDH, letrozole, and the PAAm hydrogel coating. This increasing cellular interaction and uptake due to the hydrated PAAm interface and ROS generation from Co/Mn redox cycling induce oxidative stress in cancer cells. The contributions of ROS mediation and material components in each

https://doi.org/10.1021/acsami.6c06324
ACS Appl. Mater. Interfaces 2026, 18, 36547−36565

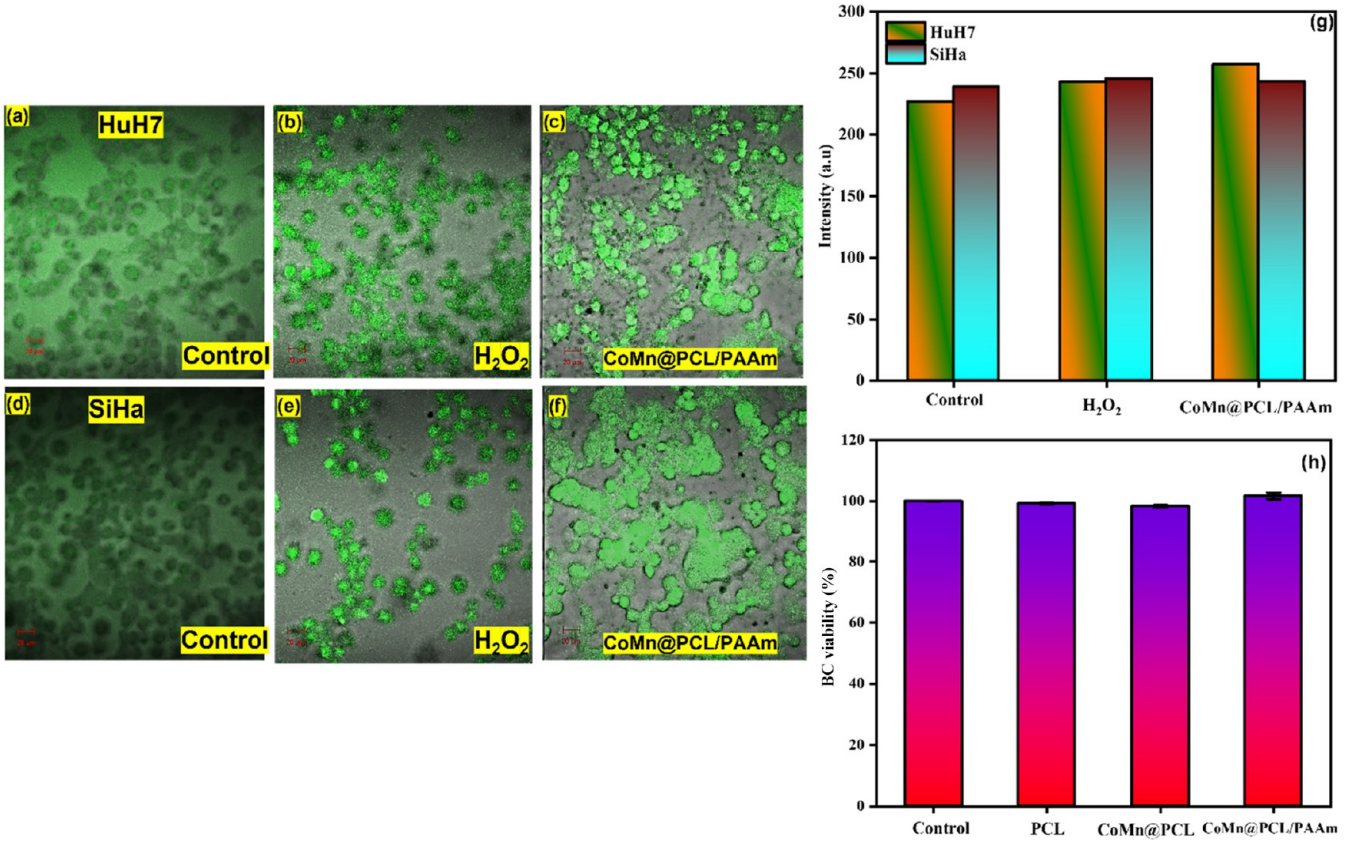

Figure 13. (a–f) ROS Assessment of CoMn@PCL/PAAm HNF against HuH7 and SiHa cells. (g) Intensity quantification of HuH7 and SiHa cells. (h) Hemocompatibility assay on CoMn@PCL/PAAm HNF.

system are calculated and presented in the Supporting Information (page S-10).

The PCL/Let system is 20.75% due to letrozole release. After incorporation of CoMn in PCL, the cell death contributed by ROS-mediated Fenton-like activity was 28.14%. However, the CoMn@PCL/PAAm/Let showed 33.23% contribution from ROS mediation and hydrogel against HuH7. The toxicity contributions of the material against HuH7 and SiHa cancer cell lines for PCL/Let, CoMn@PCL, and CoMn@PCL/PAAm are 14.86, 15.14, and 30.56%. Additionally, the hydrogel layer facilitates enhanced water diffusion and swelling, which promote drug diffusion kinetics and improve contact with the cellular membrane, thereby enhancing intracellular delivery. The comparatively higher toxicity observed in HuH7 cells is attributed to their increased susceptibility to oxidative stress, which arises from higher basal metabolic activity and lower tolerance to ROS accumulation. This may be linked to mitochondrial activity and redox imbalance, making HuH7 cells more vulnerable to ROS-induced damage, such as lipid peroxidation and DNA fragmentation. On the other hand, SiHa cells possess a more effective antioxidant defense mechanism, resulting in a comparatively lower sensitivity. Such resistance may arise from elevated levels of intracellular antioxidants (e.g., glutathione) and ROS-scavenging enzymes, which mitigate the oxidative damage (Figure 11).

3.14. In Vitro Apoptotic Cell Death Assessment by AO/EtBr Dual Staining

The dual staining assay on HuH7 and SiHa cell lines determines the apoptotic behavior of prepared NFs and HNF, as shown in Figure 12a–d. This assay differentiates the viability of cell lines on NFs and HNFs as early, late apoptotic, and necrotic conditions based on their membrane integrity and change in nuclear morphology. Acridine orange (AO) is a permeable cationic dye that penetrates any kind of cell and acts along with the nucleic acids, producing a green fluorescence in healthy nuclei. In contrast, ethidium bromide (EtBr) is only permeable to damaged plasma membranes of already compromised cells, and by binding with its DNA, it emits orange/red fluorescence. Thus, the reflection of fluorescence determines the advancement of the apoptotic stages. On evaluating the same on Let, PCL, CoMn@PCL, and CoMn@PCL/PAAm, the samples depict the stages of apoptosis. The control group of HuH7 and SiHa (Figure 12a,c) shows a homogeneous green fluorescence with perfect nuclear morphology, resulting in an active cell population with negligible apoptotic activity.

In Figure 12b,d, the cells treated against CoMn@PCL/PAAm clearly emitted a yellowish orange-red occurrence, in which EtBr has rushed into the cells due to its increased binding affinity toward the DNA of damaged cells, which have signs of shrinkage, condensation, or collapse into apoptotic bodies. This enhanced apoptotic effect can be attributed to the multifunctional contribution of sustained letrozole release, improved cellular interaction facilitated by the hydrophilic PAAm coating, and ROS generation via Co/Mn redox cycling. The oxidative stress induced by CoMn, along with effective drug release, likely disrupts mitochondrial function and induces DNA damage, leading to programmed cell death. In Figures S5 and S6a–c, the cell stage is said to be late or secondary apoptosis because the cells are in direct contact with

https://doi.org/10.1021/acsami.6c06324
ACS Appl. Mater. Interfaces 2026, 18, 36547–36565

the drug which produces a bright red fluorescence with severe membrane permeability and fragmentation (Figures S5 and S6a), whereas in Figures S5 and S6b,c, the cells show a bright green fluorescence, which indicates that the PCL and CoMn@PCL NFs are in the early stage of apoptosis likely due to mild oxidative stress induced by the CoMn phase and controlled drug release. These observations are associated with changes in membrane permeability and chromatin condensation during apoptosis.[48] Consistent with the MTT results, HuH7 cells exhibited a strong apoptotic response, which may be attributed to increased metabolic activity and reduced antioxidant defense capacity. Overall, the AO/EtBr dual-staining results confirm that CoMn@PCL/PAAm HNF induces apoptosis-mediated cell death rather than limited nonspecific necrotic damage, highlighting their potential for controlled, targeted anticancer therapy (Figure 11, Schematic presentation of Fenton-like activity).

3.15. Intracellular ROS Generation and Quantitative Fluorescence Analysis

Intracellular ROS generation was evaluated in HuH7 and SiHa cells treated with CoMn@PCL/PAAm HNF (Figure 13a–f). The control groups exhibited weak and diffuse fluorescence emission, corresponding to basal intracellular oxidative activity under normal physiological conditions. In contrast, the CoMn@PCL/PAAm-treated cells showed much stronger fluorescence, together with dense and bright domains, indicating pronounced ROS accumulation at the cell–material interface and within the intracellular environment. Moreover, fluorescence intensity quantification revealed a clear increase in both cell lines (Figure 13g), indicating that the fibrous system promotes oxidative amplification beyond peroxide exposure alone. This behavior is attributed to the redox-active Co/Mn centers within the HNF. These catalytic sites undergo Fenton-like redox cycling and promote the conversion of intracellular or supplemented H_2O_2 into highly reactive hydroxyl radicals, thereby increasing oxidative stress. The fibrous PCL matrix and hydrated PAAm hydrogel layer further support diffusion and intimate cell-material contact, enabling sustained catalytic turnover. The elevated ROS level indicates disruption of intracellular redox homeostasis, leading to lipid peroxidation, protein oxidation, and mitochondrial dysfunction, which collectively shift the cells from adaptive redox regulation toward oxidative injury and apoptosis.[49]

3.16. Hemocompatibility Assessment

The hemocompatibility of CoMn@PCL/PAAm HNF was evaluated through RBC hemolysis analysis (Figure 13h). The PCL, CoMn@PCL, and CoMn@PCL/PAAm HNF resulted in 99.23 ± 0.31%, 98.35 ± 0.35%, and 101.68 ± 1.08%, respectively. The absence of deviation from the control indicates that there is no potential membrane disruption or hemoglobin leakage, indicating that the NFs and HNF are nonhemolytic and maintain erythrocytic integrity under physiological conditions. While correlating this with ROS generation, CoMn@PCL/PAAm showed dominant ROS amplification in cancer cells; the nonhemolytic nature of the material indicates that the oxidative response is spatially and biologically regulated rather than systemically indiscriminate. The Fenton-like catalytic activity of CoMn-LDH requires enough H_2O_2 and a conductive microenvironment that can facilitate the catalytic ROS generation by the cancer cells via elevated H_2O_2 levels and redox balance. In contrast, the erythrocytes maintain a regulated antioxidant defense system and lack intracellular factors for catalytic amplifications. Thus, the CoMn@PCL/PAAm HNF has a chemically inert and stable interface with a hydrated barrier that limits direct interaction between redox-active centers and RBC membranes. This contributes to limited ROS generation in cancer cells by preserving the RBC membrane, serving as a potential therapeutic window.[50]

4. FINAL REMARK

Although letrozole is used for estrogen receptor-positive breast cancer therapy,[51] it is used as a representative for a hydrophobic anticancer drug for evaluating the drug release capacity of CoMn@PCL/PAAm HNF. The resulting anticancer activity is not only due to the contribution of the pharmacological action of letrozole but also due to the combined contribution of drug release and ROS-mediated oxidative stress generated through CoMn redox cycling. Furthermore, the previously reported literature suggests involvement of estrogen-associated signaling pathways in hepatocellular and cervical carcinomas, supporting exploratory investigations of aromatase inhibitors in these cancer models.[52]

In addition, the previously reported studies say that cobalt- and manganese-based nanomaterials exhibit acceptable biocompatibility when incorporated in controlled polymeric or nanofibrous biomedical systems. For example, the toxicological studies conducted on cobalt mentioned by Landon et al., in their review, mentioned that cobalt is a needed trace element until 1.1–1.5 mg, which is 85% available as vitamin B12. Also, the absorbed cobalt will bind with protein to 95–99% and distribute to vital organs.[53] In contrast, Yahya et al. reported that Co–Cr alloy releases ions that reduced the viability of fibroblasts to 70% at 30–40% concentration. According to ISO 10993–5, this indicates cytotoxicity. The ion further released produces oxidative stress, inflammation, and apoptosis, highlighting the risk of uncontrolled release of Co.[54] Thus, the controlled release and appropriate biomedical application of Co can be relevant without harm. For manganese, Elborolosy et al. demonstrated that Fe–Mn-based biodegradable alloys showed good biocompatibility on oral epithelial cells that improved cell proliferation over 72 h. Among the composites, the Fe–Mn–Co alloys showed good biocompatibility, indicating favorable cellular compatibility for bone-regeneration applications.[55] As with all toxic metals, the uncontrolled exposure or release of even a necessary trace element for the body can cause neurotoxicity.[56] In addition, polymer-assisted encapsulation of transition-metal nanostructures has resulted in minimal uncontrolled ion release and enhanced cellular compatibility by restricting rapid metal leaching.

Consistent with these reports, the negligible hemolytic response was observed on CoMn@PCL/PAAm HNF, as shown in Figure 13h, suggesting that the PCL/PAAm matrix may act as a protective barrier that would reduce the CoMn exposure by preserving the ROS-mediated therapeutic effect. In addition, a preliminary leachability analysis of CoMn-LDH from the CoMn@PCL/PAAm HNF was performed via an immersion technique in PBS medium at intervals of 24, 48, 72, 96, and 120 h, as shown in Figure S7. From the result, it is evident that the leaching of CoMn-LDH from the matrix is within the acceptable range, which is 0.26 μg/L of Co and 0.782 μg/L of manganese in 120 h, showing low-level metal ion diffusion from the polymer-confined nanofibrous matrix under the investigated conditions.

https://doi.org/10.1021/acsami.6c06324
ACS Appl. Mater. Interfaces 2026, 18, 36547–36565

5. CONCLUSION

In this work, the hybrid CoMn@PCL/PAAm HNFs were developed by integrating CoMn-LDH in PCL fibers, followed by PAAm hydrogel coating to produce a mechanically stable and hydrated fibrous architecture. CoMn@PCL/PAAm resulted in a multifunctional combination of diffusion-regulated drug delivery and redox-active functionality. The CoMn@PCL/PAAm HNF exhibited enhanced wettability and swelling-assisted transport, resulting in 97.3% at pH 8.8. In parallel, the redox CoMn centers promoted peroxide-activated ROS generation and improved intracellular oxidative stress, leading to apoptosis against HuH7 (64.73%) and SiHa (52.03%) cells. The system is nonhemolytic, indicating that the HNFs are blood-compatible. The hydrated fibrous scaffolds with a catalytically active inorganic phase are an effective strategy for regulating both drug transport and oxidative functionality within a single localized platform. Overall, the CoMn@PCL/PAAm HNF has a strong foundation for future development of an implantable, site-specific anticancer system with potential CDT integration and reduced toxicity.

■ ASSOCIATED CONTENT

Supporting Information

The Supporting Information is available free of charge at https://pubs.acs.org/doi/10.1021/acsami.6c06324.

Literature survey on working components of the present work, characterization, swelling ratio, drug release activity, acellular Fenton activity for ROS generation of CoMn@PCL/PAAm HNF, bacterial inhibition via resazurin assay, in vitro cancer inhibition assay, oxidative stress, leachability analysis of Co and Mn, and pictorial representation of fabricating CoMn@PCL/PAAm; Figures of Raman, XRD of PCL, and TGA of PCL, CoMn, CoMn@PCL, and CoMn@PCL NFs; Swelling ratio of PCL and CoMn@PCL and pseudo-first-order for methylene blue degradation, apoptosis analysis by HuH7 cells on PCL and CoMn@PCL, and SiHa cells on PCL and CoMn@PCL; and ROS of Letrozole and Leachability (PDF)

■ AUTHOR INFORMATION

Corresponding Authors

Ganesh Munuswamy Ramanujam − *Molecular Biology and Immunobiology Division, Interdisciplinary Institute of Indian System of Medicine (IIISM), SRM Institute of Science and Technology, Kattankulathur 603203 Tamil Nadu, India*; Email: ganeshm1@srmist.edu.in

Kun-Mu Lee − *Center for Sustainability and Energy Technologies, Chang Gung University, Taoyuan 33302, Taiwan; Department of Chemical and Materials Engineering, Chang Gung University, Taoyuan 33302, Taiwan; Division of Neonatology, Department of Pediatrics, Chang Gung Memorial Hospital, Linkou 33305, Taiwan; College of Environmental Science, Ming Chi University of Technology, New Taipei City 24301, Taiwan*; Email: kunmulee@gmail.com

Authors

Neeraja Bose − *Center for Sustainability and Energy Technologies, Chang Gung University, Taoyuan 33302, Taiwan*

Kumar Gokulkumar − *Center for Sustainability and Energy Technologies, Chang Gung University, Taoyuan 33302, Taiwan*; orcid.org/0009-0008-1944-7116

Shih-Hsuan Chen − *Center for Sustainability and Energy Technologies, Chang Gung University, Taoyuan 33302, Taiwan*

Ramalingam Mahaan − *Guangdong Basic Research Center of Excellence for Aggregate Science, School of Science and Engineering, The Chinese University of Hong Kong, Shenzhen, Guangdong 518172, P. R. China*; orcid.org/0000-0002-7722-3515

Dheepthy Fabius Suresh − *Department of Chemistry, SRM Institute of Science and Technology, Kattankulathur 603203 Tamil Nadu, India*

P Varatharajan − *Center for Sustainability and Energy Technologies, Chang Gung University, Taoyuan 33302, Taiwan*

Complete contact information is available at: https://pubs.acs.org/10.1021/acsami.6c06324

Author Contributions

○N.B., K.G- First authors and equal contribution. S.-H.C., R.M. and D.F.S- Second author. N.B.: Formal analysis, conceptualization, methodology, writing original draft, and writing—review and editing. G.K.: Schematic graphics, visualization of data, and writing review. S.-H.C.: Data collection and validation. R.M.: DFT analysis and writing—review and editing. D.F.S.: In vitro biological analysis. P.V.: visualization and validation. G.M.R.: In vitro biological analysis supervision. K.-M.L.: Funding acquisition, project administration, and supervision.

Notes

The authors declare no competing financial interest.

■ ACKNOWLEDGMENTS

The authors gratefully acknowledge financial support from the National Science and Technology Council (NSTC), Taiwan, under Project No. NSTC 111-2223-E-182-001-MY4. This research was also supported by Chang Gung University, Taiwan, under Project No (URRPD2R0011).

■ REFERENCES

(1) Wang, S.; Zou, Y.; Zhang, L.; Lv, Y. Liquid Metal-Based Nanocomposite with Triple-Amplified Fenton-like Reaction for Tumor Chemodynamic/Photothermal/Immunotherapy. *Chem. Eng. J.* **2025**, *514*, No. 163326.

(2) Hou, H.; Huang, X.; Wei, G.; Xu, F.; Wang, Y.; Zhou, S. Fenton Reaction-Assisted Photodynamic Therapy for Cancer with Multifunctional Magnetic Nanoparticles. *ACS Appl. Mater. Interfaces* **2019**, *11* (33), 29579−29592.

(3) Wu, W.; Mao, D.; Hu, F.; Xu, S.; Chen, C.; Zhang, C. J.; Cheng, X.; Yuan, Y.; Ding, D.; Kong, D.; Liu, B. A Highly Efficient and Photoss Photosensitizer with Near-Infrared Aggregation-Induced Emission for Image-Guided Photodynamic Anticancer Therapy. *Adv. Mater.* **2017**, *29* (33), No. 1700548, DOI: 10.1002/adma.201700548.

(4) Dan, Y.; He, M.; Chen, M.; Dong, C.-M. Tumor Microenvironment Stimuli-Responsive Polypeptide Manganese−Calcium Nano-

modulator Orchestrating Chemodynamic Therapy and Alleviating Hypoxia in Tumors. *ACS Appl. Bio Mater.* **2026**, *9* (6), 3050−3065.
(5) Hao, J. N.; Ge, K.; Chen, G.; Dai, B.; Li, Y. Strategies to Engineer Various Nanocarrier-Based Hybrid Catalysts for Enhanced Chemodynamic Cancer Therapy. *Chem. Soc. Rev.* **2023**, *52*, 7707−7736, DOI: 10.1039/d3cs00356f.
(6) Tang, Z.; Liu, Y.; He, M.; Bu, W. Chemodynamic Therapy: Tumour Microenvironment-Mediated Fenton and Fenton-like Reactions. *Angew. Chem.* **2019**, *131* (4), 958−968.
(7) Mei, G.; Lin, F.; Huang, L.; Lin, M.; Lin, X.; Huang, L. A PH/H2O2 Dual-Responsive Cobalt−Manganese-Based Nano-Delivery System for Chemo/Chemodynamic Therapy in Triple-Negative Breast Cancer. *Int. J. Nanomed.* **2025**, *20*, 13359−13379.
(8) Cui, Z.; Hu, T.; Yang, S.; Yang, Y.; Liu, X.; Wang, T.; Chen, H.; Zeng, C.; Liang, R.; Zhou, Y. Amorphous 2D Mn-Doped CoMo-Layered Double Hydroxide Nanosheets for Magnetic Resonance Imaging-Guided Sonodynamic Cancer Therapy. *Chem. Eng. J.* **2024**, *480*, No. 147463.
(9) Yang, H.; Chen, Z.; Guo, P.; Fei, B.; Wu, R. B-Doping-Induced Amorphization of LDH for Large-Current-Density Hydrogen Evolution Reaction. *Appl. Catal., B* **2020**, *261*, No. 118240.
(10) Sun, Y.; Gao, S.; Lei, F.; Xie, Y. Atomically-Thin Two-Dimensional Sheets for Understanding Active Sites in Catalysis. *Chem. Soc. Rev.* **2015**, *44*, 623−636, DOI: 10.1039/c4cs00236a.
(11) Zhu, Y.; Wang, Y.; Williams, G. R.; Fu, L.; Wu, J.; Wang, H.; Liang, R.; Weng, X.; Wei, M. Multicomponent Transition Metal Dichalcogenide Nanosheets for Imaging-Guided Photothermal and Chemodynamic Therapy. *Adv. Sci.* **2020**, *7* (23), No. 2000272, DOI: 10.1002/advs.202000272.
(12) Yan, L.; Wang, Y.; Hu, T.; Mei, X.; Zhao, X.; Bian, Y.; Jin, L.; Liang, R.; Weng, X.; Wei, M. Layered Double Hydroxide Nanosheets: Towards Ultrasensitive Tumor Microenvironment Responsive Synergistic Therapy. *J. Mater. Chem. B* **2020**, *8* (7), 1445−1455.
(13) Peng, L.; Mei, X.; He, J.; Xu, J.; Zhang, W.; Liang, R.; Wei, M.; Evans, D. G.; Duan, X. Monolayer Nanosheets with an Extremely High Drug Loading toward Controlled Delivery and Cancer Theranostics. *Adv. Mater.* **2018**, *30* (16), No. 1707389, DOI: 10.1002/adma.201707389.
(14) Zhang, R. Y.; Yue, W.; Xuan, Y.; Qi, L.; Guo, L. L.; Zhu, Z. Z.; Yang, M.; Pu, Z. J.; Li, G. Q.; Mao, X. Y.; Zhou, D.; Zhang, Z. W. Injectable Anti-Inflammatory Nanofiber Hydrogel Reprograms Immunosuppressive Tumor Microenvironment via Cascade-Amplified Immunogenic Cell Death. *Chem. Eng. J.* **2026**, *530*, No. 173232.
(15) Godau, B.; Samimi, S.; Seyfoori, A.; Samiei, E.; Khani, T.; Naserzadeh, P.; Najafabadi, A. H.; Lesha, E.; Majidzadeh-A, K.; Ashtari, B.; Charest, G.; Morin, C.; Fortin, D.; Akbari, M. A Drug-Eluting Injectable NanoGel for Localized Delivery of Anticancer Drugs to Solid Tumors. *Pharmaceutics* **2023**, *15* (9), No. 2255.
(16) Kim, K.; Yang, J.; Li, C.; Yang, C. Y.; Hu, P.; Liu, Y.; Huang, Y.-y.; Sun, X.; Chi, M.; Huang, C.; Sun, X.; Zhao, L.; Wang, X. Anisotropic Structure of Nanofiber Hydrogel Accelerates Diabetic Wound Healing via Triadic Synergy of Immune-Angiogenic-Neurogenic Microenvironments. *Bioact. Mater.* **2025**, *47*, 64−82.
(17) Lee, C. H.; Huang, W. Y.; Lee, K. Y.; Kuan, C. H.; Wu, T. C.; Sun, J. S.; Wang, T. W. Bioinspired Adhesive Nanofibrous Hydrogel Promotes Immune Infiltration through Effective Immunochemotherapy for Osteosarcoma Treatment. *Chem. Eng. J.* **2024**, *486*, No. 150236.
(18) Saiz-Poseu, J.; Mancebo-Aracil, J.; Nador, F.; Busqué, F.; Ruiz-Molina, D. Die Chemischen Grundlagen Der Adhäsion von Catechol. *Angew. Chem.* **2019**, *131* (3), 706−725.
(19) Cleeton, C.; Keirouz, A.; Chen, X.; Radacsi, N. Electrospun Nanofibers for Drug Delivery and Biosensing. *ACS Biomater. Sci. Eng.* **2019**, *5* (9), 4183−4205.
(20) Sennakesavan, G.; Mostakhdemin, M.; Dkhar, L. K.; Seyfoddin, A.; Fatihhi, S. J. Acrylic Acid/Acrylamide Based Hydrogels and Its Properties - A Review. *Polym. Degrad. Stab.* **2020**, *180*, No. 109308, DOI: 10.1016/j.polymdegradstab.2020.109308.
(21) Li, Q.; Zhang, L.; Liu, Z.; Yang, Y.; Guan, Y.; Liao, J.; Zhang, Y. Preparation and Performance Study of Lithium-zinc Doped Bio-Glass/Chitosan/Polyacrylamide Composite Hydrogel Loaded with Doxorubicin Hydrochloride. *Biomater. Adv.* **2026**, *180*, No. 214561.
(22) Liu, G.; Zhou, L.; Su, Y.; Dong, C.-M. An NIR-Responsive and Sugar-Targeted Polypeptide Composite Nanomedicine for Intracellular Cancer Therapy. *Chem. Commun.* **2014**, *50* (83), 12538−12541.
(23) Chavan, G. T.; Dubal, D. P.; Morankar, P. J.; Jeon, C. W.; An, J.; Song, K. H. Hierarchical CoMn-LDH and Heterostructured Composites for Advanced Supercapacitors and Electrocatalysis Applications. *Materials* **2025**, *18* (3), No. 604.
(24) Ding, B.; Ogawa, T.; Kim, J.; Fujimoto, K.; Shiratori, S. Fabrication of a Super-Hydrophobic Nanofibrous Zinc Oxide Film Surface by Electrospinning. *Thin Solid Films* **2008**, *516* (9), 2495−2501.
(25) Liang, T.; Zu, X.; Liu, B.; Qiu, X.; Xie, Z.; Wang, X.; Yang, D. A Low Temperature and High-Power Density Lignin Flow Fuel Cell via an Efficient CoMn-LDH Electrocatalyst with Superhydrophilic Intercalation. *Green Chem.* **2024**, *26* (8), 4811−4819.
(26) Liubimovskii, S. O.; Novikov, V. S.; Sagitova, E. A.; Kuznetsov, S. M.; Bakirov, A. V.; Dmitryakov, P. V.; Sedush, N. G.; Chvalun, S. N.; Ustynyuk, L. Y.; Kuzmin, V. V.; Vasimov, D. D.; Moskovskiy, M. N.; Nikolaeva, G. Y. Raman Evaluation of the Crystallinity Degree and Composition of Poly(L-Lactide-Co-ε-Caprolactone). *Spectrochim. Acta, Part A* **2024**, *310*, No. 123876.
(27) Zhang, X.; Zhang, Y.; Xie, X.; Wang, J.; Dai, S.; Qi, D.; Yu, H.; Tan, X.; Su, R.; Yan, J. AgNPs/Aramid Nanofibers-Polyacrylamide "Hill-like" Asymmetric Hydrogel Membrane as a 3D Surface-Enhanced Raman Sensor for Highly Sensitive Detection of Hazardous Residues in Food. *Sens. Actuators, B* **2026**, *458*, No. 139768.
(28) Wang, G.; Jin, M. Preparation of CoMn Layered Double Metal Oxide and Its Performance in Activating Peroxymonosulfate to Degrade Bisphenol A. *Catalysts* **2025**, *15* (10), No. 973.
(29) Castilla-Cortázar, I.; Vidaurre, A.; Marí, B.; Campillo-Fernández, A. J. Morphology, Crystallinity, and Molecular Weight of Poly(ε-Caprolactone)/Graphene Oxide Hybrids. *Polymers* **2019**, *11* (7), No. 1099.
(30) Miah, M. Y.; Halder, S.; Saikat, S. P.; Dewanjee, S.; Ashaduzzaman, M.; Bhowmik, S. Microwave-Assisted One-Step Synthesis of Polyacrylamide/NiO Nanocomposite for Biomedical Applications. *RSC Adv.* **2025**, *15* (24), 18971−18985.
(31) Roy, A.; Schoetz, T.; Gordon, L. W.; Yen, H. J.; Hao, Q.; Mandler, D. Formation of a CoMn-Layered Double Hydroxide/Graphite Supercapacitor by a Single Electrochemical Step. *ChemSusChem* **2022**, *15* (21), No. e202201418, DOI: 10.1002/cssc.202201418.
(32) Czwartos, J.; Nowak-Stępniowska, A.; Budner, B.; Fok, T.; Bartnik, A.; Wachulak, P.; Fiedorowicz, H. Polycaprolactone Scaffold Surface Modification with Soft X-Ray/Extreme Ultraviolet (SXR/EUV) Radiation and Low-Temperature Oxygen and Nitrogen Plasma for Biomedical Applications. *J. Mater. Sci.* **2024**, *59* (26), 11937−11951.
(33) Ni, T.; Huang, G. S.; Zheng, J.; Gao, P.; Chen, M. M. Research on the Crosslinking Mechanism of Polyacrylamide/Resol Using Molecular Simulation and X-Ray Photoelectron Spectroscopy. *Polym. J.* **2010**, *42* (5), 357−362.
(34) Arif, M.; Yasin, G.; Shakeel, M.; Fang, X.; Gao, R.; Ji, S.; Yan, D. Coupling of Bifunctional CoMn-Layered Double Hydroxide@Graphitic C3N4 Nanohybrids towards Efficient Photoelectrochemical Overall Water Splitting. *Chem. − Asian J.* **2018**, *13* (8), 1045−1052.
(35) Lizarazo-Fonseca, L.; Correa-Araujo, L.; Prieto-Abello, L.; Camacho-Rodríguez, B.; Silva-Cote, I. In Vitro and in Vivo Evaluation of Electrospun Poly (ε-Caprolactone)/Collagen Scaffolds and Wharton's Jelly Mesenchymal Stromal Cells (HWJ-MSCs) Constructs as Potential Alternative for Skin Tissue Engineering. *Regen. Ther.* **2023**, *24*, 11−24.
(36) Attia, M. F.; Montaser, A. S.; Arifuzzaman, M.; Pitz, M.; Jlassi, K.; Alexander-Bryant, A.; Kelly, S. S.; Alexis, F.; Whitehead, D. C. In

Situ Photopolymerization of Acrylamide Hydrogel to Coat Cellulose Acetate Nanofibers for Drug Delivery System. *Polymers* **2021**, *13* (11), No. 1863.
(37) Bao, J.; Xie, J.; Lei, F.; Wang, Z.; Liu, W.; Xu, L.; Guan, M.; Zhao, Y.; Li, H. Two-Dimensional Mn-Co LDH/Graphene Composite towards High-Performance Water Splitting. *Catalysts* **2018**, *8* (9), No. 350.
(38) Chavan, G. T.; Ingole, R. S.; Rosaiah, P.; Karim, M. R.; Park, S.; An, J. Nanoarchitectured CuAlS@CoMn-Layered Double Hydroxide Hybrids with Trimetallic Synergy for Efficient Water Splitting. *J. Power Sources* **2025**, *655*, No. 237991.
(39) Narayanan, G.; Shen, J.; Boy, R.; Gupta, B. S.; Tonelli, A. E. Aliphatic Polyester Nanofibers Functionalized with Cyclodextrins and Cyclodextrin-Guest Inclusion Complexes. *Polymers* **2018**, *10*, No. 428, DOI: 10.3390/polym10040428.
(40) Chandra, J.; Patel, J. D.; Li, J.; Zhou, G.; Mukherjee, P. K.; McCormick, T. S.; Anderson, J. M.; Ghannoum, M. A. Modification of Surface Properties of Biomaterials Influences the Ability of Candida Albicans to Form Biofilms. *Appl. Environ. Microbiol.* **2005**, *71* (12), 8795−8801.
(41) Samy, M.; Ekram, B.; El-Hady, B. M. A.; Ayoub, M. M. H. In Vitro Release Study of Electrospun Poly(ε-Caprolactone)/Gelatin Nanofiber Mats Loaded with 5-Fluorouracil. *Polym. Bull.* **2024**, *81* (5), 3953−3972.
(42) Poyraz, Y.; Baltacı, N.; Hassan, G.; Alayoubi, O.; Uysal, B. Ö.; Pekcan, Ö. Composite Hydrogel of Polyacrylamide/Starch/Gelatin as a Novel Amoxicillin Delivery System. *Gels* **2024**, *10* (10), No. 625.
(43) Luraghi, A.; Peri, F.; Moroni, L. Electrospinning for Drug Delivery Applications: A Review. *J. Controlled Release* **2021**, 463−484, DOI: 10.1016/j.jconrel.2021.03.033.
(44) Peppas, N. A.; Sahlin, J. J. A Simple Equation for the Description of Solute Release. III. Coupling of Diffusion and Relaxation. *Int. J. Pharm.* **1989**, *57* (2), 169−172.
(45) Mahani, N. m. A Dispersion-Corrected DFT Calculation on the Drug Delivery of Bezafibrate Using Pectin Biopolymer. *Sci. Rep.* **2025**, *15* (1), No. 38779, DOI: 10.1038/s41598-025-22765-x.
(46) Bose, N.; Danagody, B.; Rajappan, K.; Ramanujam, G. M.; Anilkumar, A. K. Development and Characterization of AgHNTs@SPU Film Loaded with Letrozole as Drug Delivery System and Its Anticancer Activity. *J. Drug Delivery Sci. Technol.* **2023**, *85*, No. 104557.
(47) Bose, N.; Danagody, B.; Rajappan, K.; Ramanujam, G. M.; Anilkumar, A. Silica Composites With Nickel In Situ PU/PVP Film for PH-Responsive and ROS-Stimulated Anticancer Drug Delivery System. *J. Appl. Polym. Sci.* **2025**, *142* (30), No. e57230, DOI: 10.1002/app.57230.
(48) Sahoo, B. N.; Joshi, B.; Rana, S.; Rathnam, V. S. S.; Sahare, T.; Joshi, A. Synergistic Anticancer Effect of Doxorubicin and Tamoxifen in Chitosan Nanoparticles for ER-Positive Breast Cancer. *J. Drug Delivery Sci. Technol.* **2025**, *111*, No. 107213.
(49) Iqbal, Y.; Asghar, S.; Hanif, R.; Amin, F. PMA-Coated Gold Nanoparticles Functionalized with Diamine-PEG Conjugated with Betulinic Acid for in Vitro Mitochondrial-Targeted Anticancer and ROS Detection Study against MDA-MB-231 Cell Lines. *Colloids Surf., A* **2025**, *721*, No. 137170.
(50) Bose, N.; Rajappan, K.; Natesan, G.; Selvam, S. DHNTs Assimilated TPU/PEG Membrane a New Combination for Evaluation of in-Vitro Blood-Coagulation. *Int. J. Polym. Mater. Polyme. Biomater.* **2023**, *72* (12), 925−936.
(51) Nair, H. B.; Luthra, R.; Kirma, N.; Liu, Y. G.; Flowers, L.; Evans, D.; Tekmal, R. R. Induction of Aromatase Expression in Cervical Carcinomas: Effects of Endogenous Estrogen on Cervical Cancer Cell Proliferation. *Cancer Res.* **2005**, *65* (23), 11164−11173.
(52) Guo, Y.; Wu, G.; Yi, J.; Yang, Q.; Jiang, W.; Lin, S.; Yang, X.; Cai, X.; Mao, L. Anti-Hepatocellular Carcinoma Effect and Molecular Mechanism of the Estrogen Signaling Pathway. *Front. Oncol.* **2022**, *11*, No. 763539, DOI: 10.3389/fonc.2021.763539.
(53) Landon, G.; Bouvier-Capely, C.; Fay, F.; Fattal, E.; Phan, G. Cobalt: An Update Review from Biokinetic and Toxicological Data to Treatment after Internal Exposure. *Health Phys.* **2026**, *130*, 111−125.
(54) Yahya, A. A. M.; Hosny, G.; El-Banna, S. G.; Alsakhawy, S. A. Toxicological Assessment of Cobalt-Chromium Dental Alloys: Ion Release, Cytotoxicity, and Possible Systemic Effects. *Biol. Trace Elem. Res.* **2026**, *204*, 3878−3895.
(55) Elborolosy, S. A.; Hussein, L. A.; Mahran, H.; Ammar, H. R.; Sivasankaran, S.; Abd El-Ghani, S. F.; Abdelfattah, M. Y.; Abou-Zeid, A. W.; Ibrahim, S. H.; Elshamaa, M. M. Evaluation of the Biocompatibility, Antibacterial and Anticancer Effects of a Novel Nano-Structured Fe−Mn-Based Biodegradable Alloys in-Vitro Study. *Heliyon* **2023**, *9* (11), No. e20932, DOI: 10.1016/j.heliyon.2023.e20932.
(56) Keramari, V.; Girousi, S. Manganese Nanoparticles for Heavy Metal Detection vs. Noble and Base Metal Nanoparticles; Prospects, Limitations, and Applications in Electroanalysis. *Chemosensors* **2025**, *13*, No. 313, DOI: 10.3390/chemosensors13080313.